Editors' Suggestion

Observation of Symmetry-Protected Selection Rules in Periodically Driven Quantum Systems

Guoqing Wang (王国庆),[1,*] Changhao Li (李长昊),[1,*] and Paola Cappellaro[1,2,†]
[1]Research Laboratory of Electronics and Department of Nuclear Science and Engineering, Massachusetts Institute of Technology, Cambridge, Massachusetts 02139, USA
[2]Department of Physics, Massachusetts Institute of Technology, Cambridge, Massachusetts 02139, USA

(Received 25 May 2021; revised 9 August 2021; accepted 9 September 2021; published 29 September 2021)

Periodically driven (Floquet) quantum systems have recently been a focus of nonequilibrium physics by virtue of their rich dynamics. Time-periodic systems not only exhibit symmetries that resemble those in spatially periodic systems, but also display novel behavior that arises from symmetry breaking. Characterization of such dynamical symmetries is crucial, but often challenging due to limited driving strength and lack of an experimentally accessible characterization technique. Here, we show how to reveal dynamical symmetries, namely, parity, rotation, and particle-hole symmetries, by observing symmetry-induced Floquet selection rules. Notably, we exploit modulated driving to reach the strong light-matter coupling regime, and we introduce a protocol to experimentally extract the transition matrix elements between Floquet states from the system coherent evolution. By using nitrogen-vacancy centers in diamond as an experimental test bed, we execute our protocol to observe symmetry-protected dark states and dark bands, and coherent destruction of tunneling. Our work shows how one can exploit the quantum control toolkit to study dynamical symmetries that arise in the topological phases of strongly driven Floquet systems.

DOI: 10.1103/PhysRevLett.127.140604

Symmetries play an important role in determining system properties: they can lead to intriguing physical phenomena, such as topological phases [1–7], and universality classes [8]. As an example, different phases of topological insulators have been arranged into a periodic table [1]. Engineering novel quantum materials with desired symmetry properties [2–5] can be challenging. Time-periodic systems provide an alternative solution with increased versatility, even enabling novel dynamical phases that are absent in static systems [9–14], as the periodic driving can force the system towards topological phases [15–17]. These dynamical time symmetries are described by Floquet theory [6], in analogy to the description of spatial symmetries by Bloch theory.

A hallmark of symmetries is the presence of induced selection rules. Selection rules of transitions between Floquet states have recently been analyzed theoretically [18], but their experimental observation remains challenging. First, although strong light-matter coupling is required to generate high-order Floquet bands, this regime is difficult to reach in practice due to the finite strength of the driving fields. Second, observing the selection rules requires an experimental toolkit that enables an extraction of transition elements between Floquet states. In this Letter, we tackle both challenges and provide a feasible solution by combining modulated driving with the observation of the subsequent quantum coherent dynamics, to experimentally detect symmetry-induced selection rules—and their breaking.

Recent years have witnessed a rapid development of exquisite quantum control techniques that can enable engineered driving beyond hardware limitations [19]. For example, concatenated continuous driving (CCD), originally introduced to counteract driving inhomogeneities in dynamical decoupling [20–22], has recently been shown to allow one to reach the strong-coupling regime and uncover phenomena such as high-order Mollow triplets [23] that would be "invisible" in simple driving protocols. Here we exploit modulated driving not only to achieve an effective strong-coupling regime even with limited driving strength, but also to engineer driving transitions (such as double-quantum transitions) that would otherwise not be directly accessible. To extract transition elements between Floquet states, we further develop a protocol based on monitoring the coherent state evolution by projective measurements, which enacts a mapping of the dynamical dipole matrix elements describing Floquet band transitions to measurable Rabi oscillation amplitudes. We take advantage of the controllability and long coherence times achieved in qubit-like systems [24–26], avoiding the need for dissipation and for "pump-probe" methods traditional in atomic and optical physics. Our method, also applicable to general N-level quantum systems, is thus convenient in many modern quantum platforms.

By exploiting these technical advances, we are able to experimentally study parity and particle-hole symmetries by monitoring the evolution of two levels of a nitrogen-vacancy (NV) center in diamond, under modulated driving.

Our experiments reveal the emergence of dark states and dark bands and their vanishing once the corresponding symmetries are broken—as well as coherent destruction of tunneling [27–30]. We further show that modulated driving can engineer a rotationally symmetric Hamiltonian over the NV center three levels, further indicating that our methods are broadly applicable, and exemplify an important step toward exploring topological phases that arise in Floquet systems [10].

Methods.—Spatially periodic Hamiltonians in solid-state physics can be analyzed by Bloch theory, which predicts a periodic structure in reciprocal space. Likewise, the dynamics of a periodically driven Hamiltonian $\mathcal{H}(t) = \mathcal{H}(t+T)$ is solved by Floquet theory, yielding a series of equidistant energy bands (manifolds) $\lambda^\mu + n\omega_m$ $(n \in Z)$ with Floquet eigenenergies λ^μ and frequencies $\omega_m = 2\pi/T$ [6,31]. The time-dependent Schrödinger equation is indeed equivalent to the eigenvalue problem for a time-independent Floquet matrix $[\mathcal{H}(t) - i(\partial/\partial t)]|\Phi^\mu(t)\rangle = \lambda^\mu|\Phi^\mu(t)\rangle$. The Floquet eigenstates $|\Phi^\mu(t)\rangle$ have the same period as the Hamiltonian and can be decomposed into Fourier series as $|\Phi^\mu(t)\rangle = \sum_{n=-\infty}^{+\infty} e^{-in\omega_m t}|\Phi_n^\mu\rangle$ [31]. The evolved state is then a superposition of Floquet eigenstates,

$$|\Psi(t)\rangle = \sum_\mu c^\mu e^{-it\lambda^\mu}|\Phi^\mu(t)\rangle = \sum_{\mu,n} c^\mu|\Phi_n^\mu\rangle e^{-it(n\omega_m+\lambda^\mu)}, \quad (1)$$

with the coefficients c^μ set by initial conditions at $t = 0$.

Consider a time-independent symmetry operator $\hat{\mathcal{S}}$ (rotation, parity, particle-hole, etc.) satisfying

$$\hat{\mathcal{S}}\left[\mathcal{H}(\beta_S t + t_S) - i\frac{d}{dt}\right]\hat{\mathcal{S}}^{-1} = \alpha_S\left[\mathcal{H}(t) - i\frac{d}{dt}\right], \quad (2)$$

where $\{\alpha_S, \beta_S\} \in \{1, -1\}$ and t_S define the detailed parameters of the symmetry. Then the Floquet eigenstates also have the same symmetry $|\Phi^{\mu'}(t)\rangle = \pi_\mu^S\hat{\mathcal{S}}|\Phi^\mu(\beta_S t + t_S)\rangle$, with $|\pi_\mu| = 1$, as derived in Ref. [18]. These symmetries can be probed by evaluating the susceptibility, e.g., in light scattering experiments of a probe field V, in analogy with "pump-probe" schemes common in atomic and optical physics. The susceptibility depends on the dynamical dipole matrix elements associated with the probing operator V

$$V_{\mu,\nu}^{(n)} = \frac{1}{T}\int_0^T \langle\Phi^\mu(t)|V|\Phi^\nu(t)\rangle e^{-in\omega_m t}dt, \quad (3)$$

where n denotes the energy band order. When $\hat{\mathcal{S}}^\dagger V\hat{\mathcal{S}} = \alpha_V V$, the dynamical symmetry gives rise to symmetry-protected selection rules, including symmetry-protected dark states (spDSs) for $V_{\mu,\nu}^{(n)} = 0$, symmetry-protected dark bands (spDBs) for vanishing susceptibility of complete bands, and symmetry-induced transparency (siT) due to the destructive interference between nonzero elements [18,32].

Rather than measuring the susceptibility in a pump-probe experiment [18], here we establish a general experimental method to directly measure the dipole operator V. Specifically, we draw a correspondence between the dipole matrix elements, typical of light scattering experiments, and measurable Rabi oscillation amplitudes arising in the context of coherent state evolution. We show that in a coherent system, the amplitudes of the Fourier components of $\langle V(t)\rangle$ display the desired properties (spDBs, spDSs, siT, etc.) associated with dipole matrix elements $V_{\mu,\nu}^{(n)}$.

We consider a generic N-level quantum system and introduce the spectral decomposition $V = \sum_k \mathcal{V}_k|k\rangle\langle k|$, such that the dipole matrix elements in Eq. (3) can be calculated as

$$V_{\mu,\nu}^{(n)} = \mathcal{V}_k\sum_p \langle\Phi_p^\mu|k\rangle\langle k|\Phi_{p-n}^\nu\rangle. \quad (4)$$

From Eqs. (1), (4) the expectation value of $V(t)$ is then

$$\langle V\rangle = \langle\Psi(t)|V|\Psi(t)\rangle = \sum_{\mu,\nu,n} c^{\mu*}c^\nu e^{i(\lambda^\mu-\lambda^\nu)t}e^{in\omega_m t}V_{\mu,\nu}^{(n)}. \quad (5)$$

By considering the Fourier decomposition of $\langle V\rangle$,

$$\langle V\rangle = \sum_{\mu,\nu,n}|A_{\mu,\nu}^{(n)}|\cos(\omega_{\mu,\nu}^{(n)}t + \phi_{\mu,\nu}^{(n)}), \quad (6)$$

with frequencies $\omega_{\mu,\nu}^{(n)} = n\omega_m + (\lambda^\mu - \lambda^\nu)$, we find that the Fourier amplitudes

$$A_{\mu,\nu}^{(n)} = |A_{\mu,\nu}^{(n)}|\exp(i\phi_{\mu,\nu}^{(n)}) = 2c^{\mu*}c^\nu V_{\mu,\nu}^{(n)} \quad (7)$$

can be used to extract the dipole matrix elements.

Since in general it might be difficult to directly measure the operator V, one can rely on system preparation and readout to separately monitor the overlap of the state with the eigenstates of V, i.e., $P_{|k\rangle}(t) = |\langle k|\Psi(t)\rangle|^2$. We can then analyze the "*weighted Rabi*" oscillations

$$P(t) = \sum_k \frac{\mathcal{V}_k}{\mathcal{V}}P_{|k\rangle}(t) \equiv \frac{\langle V\rangle}{\mathcal{V}}, \quad \text{with} \quad \mathcal{V} = \sum_k|\mathcal{V}_k|. \quad (8)$$

The weighted Rabi oscillations can then be decomposed into frequency components with amplitudes $a_{\mu,\nu}^{(n)} = A_{\mu,\nu}^{(n)}/\mathcal{V}$, which can be used to investigate symmetry properties. For example, consider a two-level system (TLS). The probing operator V is then a combination of Pauli operators σ_j with eigenvectors $|0_j\rangle$, $|1_j\rangle$ and normalized eigenvalues ± 1. The weighted Rabi oscillations have the form $P(t) = (1/2)[P_{|0_j\rangle}(t) - P_{|1_j\rangle}(t)]$ which can be simplified to the typical Rabi oscillations $P(t) + 1/2 = P_{|0_j\rangle}(t)$, thus clarifying

the connection of our protocol with typical Rabi measurements.

In addition to using control of the readout state to measure $P_{|k\rangle}$, we can also control the initial state to extract information about selected dipole matrix elements, by appropriately choosing the coefficients c^{μ}.

When $\mu = \nu$, all bands under the same order (n) are degenerate with frequency $n\omega_m$ (*centerbands*), and the observed Rabi component is their coherent interference with an amplitude $a_0^{(n)} = 2\sum_{\mu} |c^{\mu}|^2 V_{\mu,\mu}^{(n)}/\mathcal{V}$. Each band $V_{\mu,\mu}^{(n)}$ can also be observed individually by setting the initial condition $|c^{\mu}| = 1$ (this tuning is known as *quantum mode control*) [23].

When $\mu \neq \nu$, the off-diagonal dipole matrix elements $V_{\mu,\nu}^{(n)}$ can be mapped to the Rabi amplitudes $a_{\mu,\nu}^{(n)}$ corresponding to the bands $n\omega_m + (\lambda^{\mu} - \lambda^{\nu})$ (*sidebands*). At the degeneracy points (e.g., $\lambda^{\mu} = \lambda^{\nu}$), different sidebands interfere with each other, inducing phenomena such as the siT, or more generally the Landau-Zener-Stückelberg interferometry [42,43] and coherence destruction of tunneling (CDT) [27–30].

Results.—To demonstrate the power of combining modulated driving with weighted Rabi measurements we characterize symmetries arising in two- and three-level systems, experimentally realized using NV centers.

NV centers in diamond are atomlike solid-state defects with a triplet ground state labelled by $|m_s = 0, \pm 1\rangle$ with long-coherence time that enables their applications in quantum information science, including quantum sensing [44–48] and quantum control [15,22]. To truncate the 3-level NV center to an effective TLS, we break the $|m_s = \pm 1\rangle$ degeneracy by applying an external magnetic field with strength 239 G, and selectively use the two ground states $|m_s = 0\rangle$ and $|m_s = -1\rangle$ as logical $|0\rangle$ and $|1\rangle$ [22,23,49]. We simultaneously address an ensemble of noninteracting NV centers ($\sim 10^{10}$ qubits) to increase the signal-to-noise ratio. An arbitrary waveform generator (WX1284C) is used to generate the desired waveform for Hamiltonian engineering.

To engineer strong driving on the NV centers, we rely on the phase-modulated CCD technique [50], which has been applied previously to approach the strong-coupling regime even with limited driving fields [20–22]. As shown in Fig. 1(a), we apply a phase-modulated waveform

$$\mathcal{H} = \frac{\omega_0}{2}\sigma_z + \Omega \cos\left(\omega_0 t + \frac{2\epsilon_m}{\omega_m}\cos(\omega_m t + \phi)\right)\sigma_x, \qquad (9)$$

where $\omega_0 = (2\pi)2.20$ GHz is the qubit frequency, Ω the microwave driving strength, and ϵ_m, ω_m, ϕ are modulation parameters. In the interaction picture defined by $U = \exp\{-i((\omega_0 t/2)\sigma_z + \epsilon_m[\cos(\omega_m t + \phi)/\omega_m]\sigma_z)\}$, the Hamiltonian $\mathcal{H}_I = U^{\dagger}\mathcal{H}U - U^{\dagger}i(d/dt)U$ is

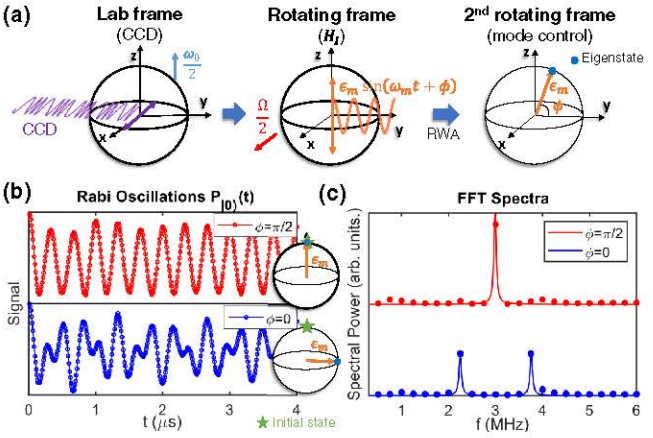

FIG. 1. (a) Sketch of the CCD technique for a TLS. (b) Rabi oscillations of $|0\rangle$ state under different modulation phases ϕ with other parameters $(\Omega, \omega_m, \epsilon_m) = (2\pi)(3, 3, 0.75)$ MHz. (c) The FFT spectra of Rabi oscillations in (b).

$$\mathcal{H}_I = \frac{\Omega}{2}\sigma_x + \epsilon_m \sin(\omega_m t + \phi)\sigma_z. \qquad (10)$$

We thus obtain a time-periodic Hamiltonian $\mathcal{H}_I$ with $T = 2\pi/\omega_m$, where Ω and ϵ_m behave as the static and driving fields, respectively, and their relative strength can be easily tuned to approach the strong coupling regime, without hardware limitations.

The periodic Hamiltonian $\mathcal{H}_I(t)$ in Eq. (10) has two nontrivial Floquet eigenenergies $\lambda^{\pm}$ and the transitions in the complete Floquet energy structure form Mollow triplets $\omega_i^{(n)} = n\omega_m + i(\lambda^{+} - \lambda^{-})$. Here $i = 0, \pm 1$ correspond to the centerbands and sidebands, respectively. These transitions can be probed either through conventional pump-probe spectroscopy, such as spontaneous emission [51], or via projective Rabi measurements in the context of coherent state evolution [23,33,52], where the Rabi amplitudes can be exactly mapped to the dipole matrix element (Table I). Under a weak-coupling regime, the Floquet eigenenergies and eigenstates can also be analytically obtained in a second rotating frame as shown in Fig. 1(a). Figures 1(b),1(c) show instances of the Rabi measurement in time and frequency domains where different Mollow bands are separately measured under different initial conditions.

In the following, we experimentally evaluate the dynamical symmetries of the qubit Hamiltonian $\mathcal{H}_I$, and study the associated spDSs, spDBs, and siT through the intensities of the Floquet state transitions, which are extracted from Rabi oscillations.

The first dynamical symmetry is a twofold rotation or parity symmetry defined by $\hat{R} = \sigma_x$, which satisfies $\hat{R}\mathcal{H}_I(t + T/2)\hat{R}^{\dagger} = \mathcal{H}_I(t)$. The selection rules are then given by $V_{\mu,\nu}^{(n)} \propto [1 + e^{i\pi(m_{\mu} - m_{\nu}) - i\pi n}\alpha_V^{(R)}]$, where $\mu \in \{+, -\}$, $m_{\mu} \in \{0, 1\}$, and the constant $\alpha_V^{(R)}$ satisfies $\hat{R}^{\dagger}V\hat{R} = \alpha_V^{(R)}V$.

TABLE I. Correspondence between the Rabi amplitudes $a_i^{(n)}$ and dipole matrix element $V_{\mu,\nu}^{(n)}$ for a TLS. Note that $\Phi_{p,0_j}^{\mu} = \langle 0_j | \Phi_p^{\mu} \rangle$, and listed cases do not include $i = n = 0$ [23,32].

Bands$_{\{i,n\}}$	Rabi amplitudes $a_{\mu,\nu}^{(n)}$	Expressed in $V_{\mu,\nu}^{(n)}$
$\{0, n\}$	$2\sum_{\pm} \lvert c^{\pm}\rvert^2 \sum_k \Phi_{k+n,0_j}^{\pm *} \Phi_{k,0_j}^{\pm}$	$\lvert c^{+}\rvert^2 V_{+,+}^{(n)} + \lvert c^{-}\rvert^2 V_{-,-}^{(n)}$
$\{-1, n\}$	$2\sum_k c^{+} c^{-*} \Phi_{k,0_j}^{+} \Phi_{k+n,0_j}^{-*}$	$c^{+} c^{-*} V_{-,+}^{(n)}$
$\{+1, n\}$	$2\sum_k c^{+*} c^{-} \Phi_{k+n,0_j}^{+*} \Phi_{k,0_j}^{-}$	$c^{+*} c^{-} V_{+,-}^{(n)}$

For observation operators that anticommute with the symmetry operator ($V = \sigma_y, \sigma_z$), the Mollow center bands with even orders and sidebands with odd orders vanish. The opposite holds for the commuting observation operator ($V = \sigma_x$). As a result, a series of spDSs and spDBs are predicted by the parity symmetry.

To experimentally observe these selection rules, we measure the Rabi oscillations under different modulation strengths $2\epsilon_m/\omega_m$ and plot their Fourier spectrum. In Figs. 2(a),2(b), the 1st, 3rd, 5th Mollow sidebands, and 2nd, 4th Mollow centerbands have vanishing intensities, as indicated by dashed lines and labels where nonzero transition amplitudes would otherwise have been expected. In Figs. 2(c),2(d), the opposite behavior is observed. These results validate the theoretical analysis. Note that some unexpected bands [e.g., odd order centerbands in the range of $2.5 < 2\epsilon_m/\omega_m < 5$ in Figs. 2(c),2(d)] are still visible, albeit with small intensities. We attribute their occurrence to experimental imperfections such as inhomogeneities that introduce a detuning term in the Hamiltonian $\mathcal{H}_I$ [22,32].

The second symmetry is a particle-hole symmetry defined by $\hat{P}_1 = \sigma_z$, which satisfies $\hat{P}_1 \mathcal{H}_I(t + T/2) \hat{P}_1^{\dagger} = -\mathcal{H}_I(t)$. The selection rules are then given by $V_{\mu,\nu}^{(n)} = \alpha_V^{(P_1)} e^{i\pi n} V_{\nu',\mu'}^{(n)}$, where $\alpha_V^{(P_1)}$ satisfies $\hat{P}_1^{\dagger} V \hat{P}_1 = \alpha_V^{(P_1)} V^*$ [53]. For sidebands, the selection rules are consistent with the parity symmetry predictions as observed in Figs. 2(a)–2(d). For centerbands, destructive interference is induced when $\alpha_V^{(P_1)} e^{i\pi n} = -1$ and the initial state is an equal superposition of two eigenstates such that $V_{+,+}^{(n)} + V_{-,-}^{(n)} = 0$. This property gives rise to vanishing centerbands in the *quantum mode control* as shown in Fig. 1(c) and Ref. [23]. For a modulation phase $\phi = 0$, the Floquet eigenstates are in the $x - y$ plane of the Bloch sphere such that $\lvert c^{\pm}\rvert^2 = 1/2$ for the initial state $\lvert 0\rangle$, and the destructive interference transpires in the odd (even) centerband when $V = \sigma_z$ ($V = \sigma_x$). Combining with the parity symmetry that makes the opposite orders of centerband vanish, all centerbands vanish under $\phi = 0$ as observed in Figs. 2(a),2(c). Instead, under the modulation phase

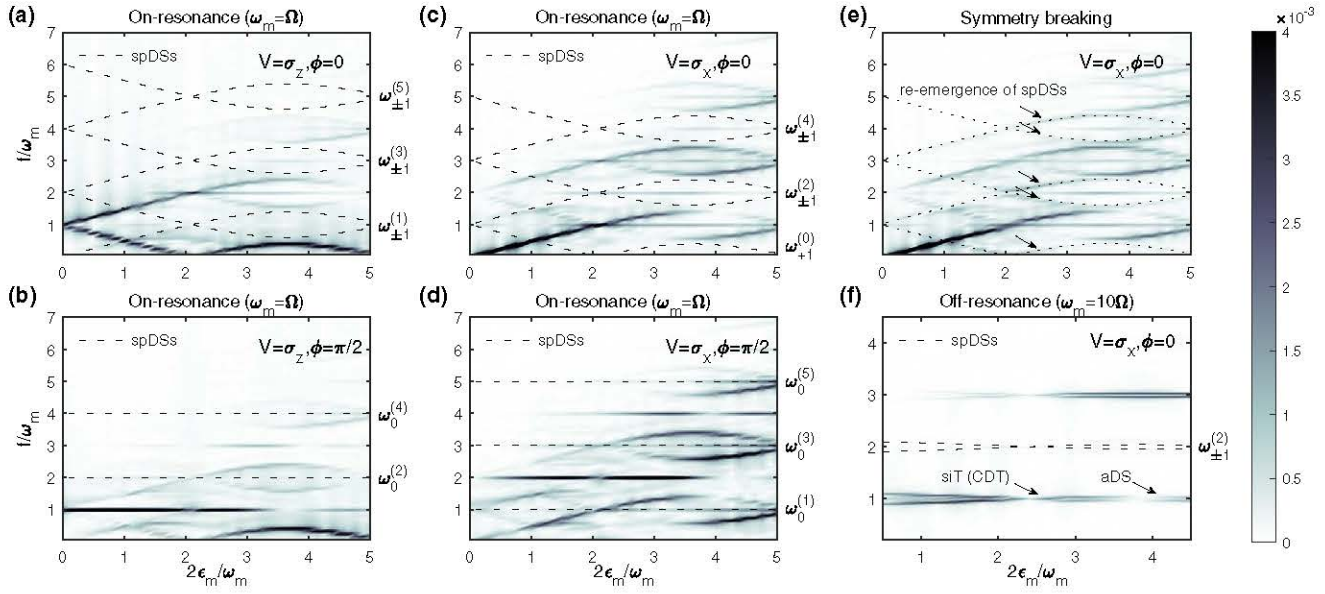

FIG. 2. Experimental observation of spDSs, spDBs, and siT. (a)–(d) Observation of spDSs, spDBs under resonant modulation $\omega_m = \Omega = (2\pi)3$ MHz. The initial state is $\lvert 0\rangle$, and we measure generalized Rabi oscillations $P_{|0\rangle}(t)$ or $P_{|+\rangle}(t)$ under different modulation strength $2\epsilon_m/\omega_m$, from 0 to 4 μs with 401 sampling points (see Fig. 1.) The plots are the Fourier spectrum of the Rabi measurements for specified modulation phases ϕ and probe operator V. In (a) the odd sidebands vanish (spDSs, marked by dashed lines and labels). Similarly, we observe vanishing even (b) and odd (d) centerbands. The even sidebands vanish in (c), but they reemerge in (e) (arrows and dotted lines), due to symmetry breaking induced by adding a perturbation, $\mathcal{H}' = 0.2\epsilon_m \sin(2\omega_m t)\sigma_z$ to the periodic Hamiltonian. (f) Observations of siT, spDSs, spDBs and accidental dark states (aDS) under off-resonant modulation ω_m, $10\Omega = (2\pi)15$ MHz (labels indicate the revealing features). Rabi oscillations $P_{|+\rangle}(t)$ of an initial state $\lvert 0\rangle$ are measured from 0 to 2 μs with 401 sampling points.

$\phi = \pi/2$, the Floquet eigenstates are in the $x-z$ plane and the condition $|c^{\pm}|^2 = 1/2$ is not always satisfied. The symmetry-allowed centerbands appear as shown in Figs. 2(b),2(d) and vanish at $2\epsilon_m/\omega_m \approx 4$, where $|c^{\pm}|^2 = 1/2$ is accidentally satisfied.

To further demonstrate the symmetry-protected selection rules, we break both the parity and particle-hole symmetries by introducing an additional term $0.2\epsilon_m \sin(2\omega_m t)\sigma_z$ in the Hamiltonian $\mathcal{H}_I$, and measure the Rabi spectrum in Fig. 2(e), where we see the emergence of all sidebands [odd allowed sidebands as in Fig. 2(c) and symmetry-breaking even sidebands.]

Another type of destructive interference, siT, is observable when sidebands interfere destructively at degeneracy points, which requires two discrete particle-hole symmetries in the system. In the strong coupling and far off-resonance regime ($\Omega \ll \epsilon_m$, ω_m), an additional particle-hole symmetry $\hat{P}_2 = I$ arises such that $I\mathcal{H}_I(t+T/2)I = -\mathcal{H}_I(t)$, which results in a relation between two sidebands $V^{(n)}_{+,-} = \alpha_V^{(P_1^*)} e^{i\pi n} V^{(n)}_{-,+}$ with $\alpha_V^{(P_1^*)}$ given by $\alpha_V^{(P_1^*)} V = \hat{P}_1{}^{\dagger *} V \hat{P}_1{}^{*}$. Under the initial condition $c^+c^{-*} = c^{+*}c^-$, the siT happens when $\alpha_V^{(P_1^*)} e^{i\pi n} = -1$, and the qubit evolution is suppressed in the direction of the driving field (the CDT effect, which has been observed before both numerically [29] and experimentally [30].) In Fig. 2(f), we engineer a strong-coupling Hamiltonian and measure the Rabi spectrum. The siT is observed when two sidebands are degenerate at $2\epsilon_m/\omega_m = 2.4048$ (see Supplemental Material for a constructive interference [32]). In addition, spDSs are also observed as in Fig. 2(c).

In order to demonstrate that our technique can be extended beyond TLSs, we show how to use the 3 levels associated with the spin-1 of NV centers to explore a threefold rotation symmetry. We use modulated driving to both reach the strong driving regime and to engineer the double quantum (DQ) transition ($|m_S = -1\rangle \leftrightarrow |m_S = +1\rangle$) in the rotating frame. Indeed, the DQ transition cannot be directly generated by microwave driving (although it could be achieved by mechanical oscillations 54,55]].) Here we overcome this limitation by simultaneously applying two modulated driving on the single quantum transitions ($|m_S = 0\rangle \leftrightarrow |m_S = \pm 1\rangle$), leading to the rotating-frame Hamiltonian [32]

$$\mathcal{H}_I^3(t) = J[\cos(\omega_m t)|-1\rangle\langle+1| + \cos(\omega_m t + 2\pi/3)|+1\rangle\langle 0| + \cos(\omega_m t + 4\pi/3)|-1\rangle\langle 0| + \text{H.c.}] \quad (11)$$

with a threefold rotation symmetry $\hat{R}\mathcal{H}_I^3(t+T/3)\hat{R}^\dagger = \mathcal{H}_I(t)$, where the rotation $\hat{R} = |-1\rangle\langle 0| + |0\rangle\langle+1| + |+1\rangle\langle -1|$. We find symmetry-protected selections rules by evaluating the Floquet eigenstates and the observation operator [32]. In Fig. 3, we simulate the Fourier spectrum of the weighted Rabi signal for the probe operator $V = |0\rangle\langle+1| + |0\rangle\langle-1| + |+1\rangle\langle-1| + \text{H.c.}$, which clearly displays the expected spDSs, protected by the threefold rotation symmetry.

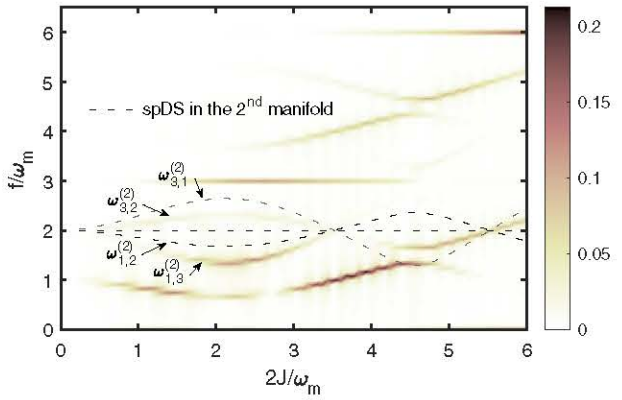

FIG. 3. Simulation of spDSs and spDBs in a three-level system (vanishing intensities marked by the dashed lines). The initial state is $(1/\sqrt{3})(|e_1\rangle + |e_2\rangle + |e_3\rangle)$ where $|e_{1,2,3}\rangle$ are eigenstates of V, such that evolution mode involves all bands. The weighted Rabi $P(t) = (1/4)[2P_{|e_1\rangle}(t) - P_{|e_2\rangle}(t) - P_{|e_3\rangle}(t)]$ is simulated from 0 to 40 μs with 5001 sampling points and the modulation frequency is 0.3 MHz.

Discussions and conclusion.—By combining modulated driving and detection via Rabi oscillations, we are able to experimentally observe selection rules protected by dynamical symmetries in a periodically driven solid-state system. The modulated driving scheme is instrumental to reach the strong light-matter coupling regime used to reveal high-order Floquet bands; it also introduces additional flexibility in quantum control, enabling one to engineer transitions forbidden in the unmodulated frame and reveal details of the dynamics (e.g., Mollow triplets) via mode control. Direct measurement of the dipolar transition operator V, or indirectly via weighted Rabi oscillations is a more efficient strategy than previous pump-probe methods in the highly coherent quantum systems that can now be routinely engineered. In virtue of these techniques, we characterized the time-domain parity and particle-hole symmetries as well as the CDT effect in the engineered system. In the context of quantum control, the dynamical symmetries studied here have applications in inducing selections rules for higher harmonic generation and driving quantum synchronization [56–59].

While we showed simulations and experiments for two- and three-level systems, the experimental techniques we introduced can be generalized to many-body (N-level) systems in a broad set of platforms beyond spins, such as cold atoms and superconducting circuits.

When combined with spatial symmetries, dynamical symmetries characterized in this work can lead to novel Floquet topological phases such as Floquet topological insulators and superconductors [10]. The breaking of these dynamical symmetries might lead to intriguing dynamical phase transitions. Furthermore, by engineering of the dissipation such as tuning the decoherence rate of the

system, the work here paves the way towards further exploration of non-Hermitian Floquet Hamiltonians.

This work was in part supported by ARO Grant No. W911NF-11-1-0400 and NSF Grants No. PHY1734011 and No. EECS1702716. We thank Pai Peng for fruitful discussions and Thanh Nguyen for manuscript revision.

*These authors contributed equally to this work.
†pcappell@mit.edu

[1] A. Kitaev, AIP Conf. Proc. **1134**, 22 (2009).
[2] M. Angeli and A. H. MacDonald, Proc. Natl. Acad. Sci. U.S.A. **118**, e2021826118 (2021).
[3] Y. Cao, V. Fatemi, S. Fang, K. Watanabe, T. Taniguchi, E. Kaxiras, and P. Jarillo-Herrero, Nature (London) **556**, 43 (2018).
[4] K. L. Seyler, P. Rivera, H. Yu, N. P. Wilson, E. L. Ray, D. G. Mandrus, J. Yan, W. Yao, and X. Xu, Nature (London) **567**, 66 (2019).
[5] K. Tran, G. Moody, F. Wu, X. Lu, J. Choi, K. Kim, A. Rai, D. A. Sanchez, J. Quan, A. Singh, J. Embley, A. Zepeda, M. Campbell, T. Autry, T. Taniguchi, K. Watanabe, N. Lu, S. K. Banerjee, K. L. Silverman, S. Kim, E. Tutuc, L. Yang, A. H. MacDonald, and X. Li, Nature (London) **567**, 71 (2019).
[6] J. H. Shirley, Phys. Rev. **138**, B979 (1965).
[7] X.-L. Yu, W. Ji, L. Zhang, Y. Wang, J. Wu, and X.-J. Liu, PRX Quantum **2**, 020320 (2021).
[8] G. Ódor, Rev. Mod. Phys. **76**, 663 (2004).
[9] A. Eckardt, Rev. Mod. Phys. **89**, 011004 (2017).
[10] R. Roy and F. Harper, Phys. Rev. B **96**, 155118 (2017).
[11] Y. Peng and G. Refael, Phys. Rev. Lett. **123**, 016806 (2019).
[12] K. Wintersperger, C. Braun, F. N. Ünal, A. Eckardt, M. D. Liberto, N. Goldman, I. Bloch, and M. Aidelsburger, Nat. Phys. **16**, 1058 (2020).
[13] P. Peng, C. Yin, X. Huang, C. Ramanathan, and P. Cappellaro, Nat. Phys. **17**, 444 (2021).
[14] C. Yin, P. Peng, X. Huang, C. Ramanathan, and P. Cappellaro, Phys. Rev. B **103**, 054305 (2021).
[15] M. C. Rechtsman, J. M. Zeuner, Y. Plotnik, Y. Lumer, D. Podolsky, F. Dreisow, S. Nolte, M. Segev, and A. Szameit, Nature (London) **496**, 196 (2013).
[16] G. Jotzu, M. Messer, R. Desbuquois, M. Lebrat, T. Uehlinger, D. Greif, and T. Esslinger, Nature (London) **515**, 237 (2014).
[17] K. Jiménez-García, L. J. LeBlanc, R. A. Williams, M. C. Beeler, C. Qu, M. Gong, C. Zhang, and I. B. Spielman, Phys. Rev. Lett. **114**, 125301 (2015).
[18] G. Engelhardt and J. Cao, Phys. Rev. Lett. **126**, 090601 (2021).
[19] A. Ajoy, Y.-X. Liu, K. Saha, L. Marseglia, J.-C. Jaskula, U. Bissbort, and P. Cappellaro, Proc. Natl. Acad. Sci. U.S.A. **114**, 2149 (2017).
[20] J.-M. Cai, B. Naydenov, R. Pfeiffer, L. P. McGuinness, K. D. Jahnke, F. Jelezko, M. B. Plenio, and A. Retzker, New J. Phys. **14**, 113023 (2012).
[21] D. Farfurnik, N. Aharon, I. Cohen, Y. Hovav, A. Retzker, and N. Bar-Gill, Phys. Rev. A **96**, 013850 (2017).
[22] G. Wang, Y.-X. Liu, and P. Cappellaro, New J. Phys. **22**, 123045 (2020).
[23] G. Wang, Y.-X. Liu, and P. Cappellaro, Phys. Rev. A **103**, 022415 (2021).
[24] E. Bauch, C. A. Hart, J. M. Schloss, M. J. Turner, J. F. Barry, P. Kehayias, S. Singh, and R. L. Walsworth, Phys. Rev. X **8**, 031025 (2018).
[25] M. Zhong, M. P. Hedges, R. L. Ahlefeldt, J. G. Bartholomew, S. E. Beavan, S. M. Wittig, J. J. Longdell, and M. J. Sellars, Nature (London) **517**, 177 (2015).
[26] S. Ebadi, T. T. Wang, H. Levine, A. Keesling, G. Semeghini, A. Omran, D. Bluvstein, R. Samajdar, H. Pichler, W. W. Ho, S. Choi, S. Sachdev, M. Greiner, V. Vuletić, and M. D. Lukin, Nature (London) **595**, 227 (2021).
[27] F. Grossmann, T. Dittrich, P. Jung, and P. Hänggi, Phys. Rev. Lett. **67**, 516 (1991).
[28] F. Grossmann, T. Dittrich, P. Jung, and P. Hänggi, J. Stat. Phys. **70**, 229 (1993).
[29] Z. Lü and H. Zheng, Phys. Rev. A **86**, 023831 (2012).
[30] J. Zhou, P. Huang, Q. Zhang, Z. Wang, T. Tan, X. Xu, F. Shi, X. Rong, S. Ashhab, and J. Du, Phys. Rev. Lett. **112**, 010503 (2014).
[31] M. Leskes, P. Madhu, and S. Vega, Prog. Nucl. Magn. Reson. Spectrosc. **57**, 345 (2010).
[32] See Supplemental Material at http://link.aps.org/supplemental/10.1103/PhysRevLett.127.140604 for details, which includes Refs. [18,20–23,31,33–41].
[33] S. Rohr, E. Dupont-Ferrier, B. Pigeau, P. Verlot, V. Jacques, and O. Arcizet, Phys. Rev. Lett. **112**, 010502 (2014).
[34] N. Khaneja, A. Dubey, and H. S. Atreya, J. Magn. Reson. **265**, 117 (2016).
[35] A. Saiko, R. Fedaruk, and S. Markevich, J. Magn. Reson. **290**, 60 (2018).
[36] I. Cohen, N. Aharon, and A. Retzker, Fortschr. Phys. **65**, 1600071 (2017).
[37] K. J. Layton, B. Tahayori, I. M. Mareels, P. M. Farrell, and L. A. Johnston, J. Magn. Reson. **242**, 136 (2014).
[38] A. P. Saiko, R. Fedaruk, and S. A. Markevich, J. Magn. Reson. **259**, 47 (2015).
[39] J. Teissier, A. Barfuss, and P. Maletinsky, J. Opt. **19**, 044003 (2017).
[40] S. Bertaina, H. Vezin, H. De Raedt, and I. Chiorescu, Sci. Rep. **10**, 21643 (2020).
[41] Q.-Y. Cao, P.-C. Yang, M.-S. Gong, M. Yu, A. Retzker, M. B. Plenio, C. Müller, N. Tomek, B. Naydenov, L. McGuinness, F. Jelezko, and J.-M. Cai, Phys. Rev. Applied **13**, 024021 (2020).
[42] S. Shevchenko, S. Ashhab, and F. Nori, Phys. Rep. **492**, 1 (2010).
[43] P. Huang, J. Zhou, F. Fang, X. Kong, X. Xu, C. Ju, and J. Du, Phys. Rev. X **1**, 011003 (2011).
[44] C. L. Degen, F. Reinhard, and P. Cappellaro, Rev. Mod. Phys. **89**, 035002 (2017).
[45] R. Schirhagl, K. Chang, M. Loretz, and C. L. Degen, Annu. Rev. Phys. Chem. **65**, 83 (2014).
[46] C. Li, M. Chen, D. Lyzwa, and P. Cappellaro, Nano Lett. **19**, 7342 (2019).
[47] S. Schmitt, T. Gefen, F. M. Stürner, T. Unden, G. Wolff, C. Müller, J. Scheuer, B. Naydenov, M. Markham,

S. Pezzagna, J. Meijer, I. Schwarz, M. Plenio, A. Retzker, L. P. McGuinness, and F. Jelezko, Science **356**, 832 (2017).

[48] G. Wang, Y.-X. Liu, Y. Zhu, and P. Cappellaro, Nano Lett. **21**, 5143 (2021).

[49] J.-C. Jaskula, K. Saha, A. Ajoy, D. J. Twitchen, M. Markham, and P. Cappellaro, Phys. Rev. Applied **11**, 054010 (2019).

[50] Here we did not choose amplitude-modulated CCD, since it is still limited by the total microwave power and amplifier nonlinearity [23].

[51] B. R. Mollow, Phys. Rev. **188**, 1969 (1969).

[52] B. Pigeau, S. Rohr, L. Mercier de Lépinay, A. Gloppe, V. Jacques, and O. Arcizet, Nat. Commun. **6**, 8603 (2015).

[53] The particle-hole symmetry operator $\hat{P}_1$ here maps one eigenstate to its counterpart such that $\mu' = \mp$ corresponding to $\mu = \pm$.

[54] E. R. MacQuarrie, T. A. Gosavi, A. M. Moehle, N. R. Jungwirth, S. A. Bhave, and G. D. Fuchs, Optica **2**, 233 (2015).

[55] E. R. MacQuarrie, T. A. Gosavi, N. R. Jungwirth, S. A. Bhave, and G. D. Fuchs, Phys. Rev. Lett. **111**, 227602 (2013).

[56] J. Tindall, C. S. Muñoz, B. Buča, and D. Jaksch, New J. Phys. **22**, 013026 (2020).

[57] O. E. Alon, Phys. Rev. A **66**, 013414 (2002).

[58] O. E. Alon, V. Averbukh, and N. Moiseyev, Phys. Rev. Lett. **85**, 5218 (2000).

[59] O. E. Alon, V. Averbukh, and N. Moiseyev, Phys. Rev. Lett. **80**, 3743 (1998).

Supplemental materials: Observation of symmetry-protected selection rules in periodically driven quantum systems

Guoqing Wang (王国庆),[1,*] Changhao Li (李长昊),[1,*] and Paola Cappellaro[1,2,†]

[1] *Research Laboratory of Electronics and Department of Nuclear Science and Engineering, Massachusetts Institute of Technology, Cambridge, MA 02139, USA*

[2] *Department of Physics, Massachusetts Institute of Technology, Cambridge, MA 02139, USA*

CONTENTS

* These authors contributed equally.
† pcappell@mit.edu

I. DYNAMICS OF A PERIODICALLY DRIVEN QUANTUM SYSTEM

In this section we introduce the basics of Floquet theory as well as the concatenated continuous driving technique. While many of the definitions and results below have been presented in reference [1] (and elsewhere), we briefly reiterate them here for convenience.

A. Floquet theory

1. General derivation

We first give the detailed steps to solve the Floquet problem [2]. Given a time-periodic Hamiltonian $\mathcal{H}(t) = \mathcal{H}(t+2\pi/\omega)$, its eigenstates have the form $|\Psi(t)\rangle = e^{-i\lambda t}|\Phi(t)\rangle$, where $|\Phi(t)\rangle = |\Phi(t+2\pi/\omega)\rangle$ is periodic in time and λ denotes the eigenenergy. The Schrödinger equation $i\frac{\partial}{\partial t}|\Psi(t)\rangle = H(t)|\Psi(t)\rangle$ is then equivalent to

$$\left(H(t) - i\frac{\partial}{\partial t}\right)|\Phi(t)\rangle = \lambda|\Phi(t)\rangle. \tag{S1}$$

Plugging the Fourier expansions $|\Phi(t)\rangle = \sum_n |\Phi_n\rangle e^{-in\omega t}$, $H(t) = \sum_n H_n e^{-in\omega t}$ into Eq. (S1), we obtain

$$\left(\sum_n H_n(t)e^{-in\omega t} - i\frac{\partial}{\partial t}\right)\sum_p |\Phi_p\rangle e^{-im\omega t} = \lambda\sum_p |\Phi_p\rangle e^{-im\omega t}. \tag{S2}$$

This can be expressed in matrix form as $\mathcal{H}_F\vec{\Phi} = \lambda\vec{\Phi}$,

$$\begin{pmatrix} \ddots & \vdots & 0 & \vdots & \\ \cdots & H_0+\omega & H_{-1} & 0 & \cdots \\ \cdots & H_1 & H_0 & H_{-1} & \\ \cdots & 0 & H_1 & H_0-\omega & \cdots \\ & \vdots & \vdots & \vdots & \ddots \end{pmatrix}\begin{bmatrix} \vdots \\ \Phi_{-1} \\ \Phi_0 \\ \Phi_1 \\ \vdots \end{bmatrix} = \lambda\begin{bmatrix} \vdots \\ \Phi_{-1} \\ \Phi_0 \\ \Phi_1 \\ \vdots \end{bmatrix}, \tag{S3}$$

which defines the Floquet matrix $\mathcal{H}_F$.

Given the Floquet matrix eigenenergies λ^μ and eigenvectors $\vec{\Phi}^\mu = (\cdots, \Phi^\mu_{-1}, \Phi^\mu_0, \Phi^\mu_1, \cdots)^T$, the state evolution of the system is a superposition of these eigenvectors

$$|\Psi(t)\rangle = \sum_\mu c^\mu |\Psi^\mu(t)\rangle = \sum_\mu c^\mu e^{-i\lambda^\mu t}\sum_{n=-\infty}^{+\infty} e^{-in\omega t}|\Phi^\mu_n\rangle \tag{S4}$$

with coefficients c^μ determined by the initial condition

$$|\Psi(t=0)\rangle = \sum_\mu c^\mu \sum_{n=-\infty}^{+\infty}|\Phi^\mu_n\rangle. \tag{S5}$$

a. Quasi energy. Given an eigenenergy λ^μ, $\lambda^\mu + n\omega$ for any integer n is also an eigenenergy since $|\Psi^\mu(t)\rangle = e^{-i\lambda^\mu t}|\Phi^\mu(t)\rangle = e^{-i\lambda^\mu t - in\omega t}(e^{in\omega t}|\Phi^\mu(t)\rangle)$. To simplify the calculation, we usually limit the range of the eigenvalues within the first "Brillouin zone" $(-\omega/2, \omega/2]$. Note that the definition of "Brillouin zone" is flexible and in Ref. [1] it is defined as $(0, \omega]$ to comply with the conventional definition of Mollow triplets. In this work, we pick $(-\omega/2, \omega/2]$ to make it easier to analyze the particle-hole symmetry, where two eigenvalues have a symmetry-induced relation $\lambda^- = -\lambda^+$.

b. Number of nontrivial eigenvalues in an N-level quantum system. For an N-level quantum system, the Hamiltonian $\mathcal{H}(t)$ is an $N \times N$ matrix, while state vectors $|\Psi(t)\rangle$, $|\Phi(t)\rangle$ and their the Fourier components $|\Phi_n\rangle$, are $N \times 1$ vectors, which can also be equivalently written as $|\Psi(t)\rangle, |\Phi(t)\rangle$. In Floquet space, there are N non-trivial eigenvalues (in the first Brillouin zone) denoted by λ^μ, while all the other eigenvalues are simple translations of these values with $\lambda^\mu + n\omega$.

c. Number of nontrivial eigenvalues in a qubit system. For qubit systems, the Hamiltonian $\mathcal{H}(t)$ are 2×2 matrices, eigenstates $|\Psi(t)\rangle$, $|\Phi(t)\rangle$ and the Fourier components $|\Phi_n\rangle$, are 2×1 vectors which can also be equivalently written as $|\Psi(t)\rangle, |\Phi(t)\rangle$. Due to the equidistant energy structures of a Floquet problem, there are two non-trivial eigenvalues denoted by $\lambda^{\pm}$ for a 2-level system and all the other eigenvalues are simple translation of these two values with $\lambda^{\pm}+n\omega$.

d. Truncation in numerical simulations. Since the Floquet matrix $\mathcal{H}_F$ has infinite dimension, in this work we truncate the matrix to 400×400 blocks in the numerical simulation for the 2-level system, and to (300×300) blocks for the 3-level system. In Figs. S12(e-h) we compare the Floquet simulation to a simulation based on a Trotterized evolution, and show that the Floquet solution overlaps perfectly with the Trotter solution. Note that in the Trotterized evolution, we discretize the time into small steps $dt=0.0004\mu$s ($dt=0.008, 0.00025\mu$s for Figs. S14(a,c)) and calculate the evolution by multiplying the time series of e^{-iHdt} with the Hamiltonian in $\mathcal{H}_I$.

We used Floquet simulations for the plots of eigenstates in the Bloch sphere, to calculate Floquet eigenvalues and the parameters π_μ. All other simulations in this work were done by the using the Trotterized evolution, although the Floquet simulation has similar precision and efficiency.

2. *Generalized Rabi amplitudes*

Although the Rabi oscillation is typically defined for a(n effective) two-level system (e.g., measurement of $P_{|0\rangle}(t)$ for a qubit), a generalized Rabi oscillation $P_{|k\rangle}(t)$ can be defined for an N-level system where k denotes the projection state. With Floquet theory, such a Rabi oscillation for an initial state described by coefficients c^μ's can be calculated as

$$\begin{aligned} P_{|k\rangle}(t) &= \sum_n e^{-in\omega t}\sum_\mu c^\mu e^{-i\lambda^\mu t}\Phi^\mu_{n,k}\times\sum_p e^{im\omega t}\sum_\nu c^{\nu*}e^{i\lambda^\nu t}\Phi^{\nu*}_{p,k} \\ &= \sum_{n,p} e^{i(p-n)\omega t}\left(\sum_\mu |c^\mu|^2\Phi^{\mu*}_{p,k}\Phi^\mu_{n,k}+\sum_{\mu,\nu\neq\mu} e^{-i(\lambda^\mu-\lambda^\nu)t}c^\mu c^{\nu*}\Phi^\mu_{n,k}\Phi^{\nu*}_{p,k}\right), \end{aligned} \tag{S6}$$

We can rewrite this expression as

$$P_{|k\rangle}(t)=\sum_{\mu,\nu,n}|a^{(n,k)}_{\mu,\nu}|\cos\left(\omega^{(n)}_{\mu,\nu}t+\phi^{(n,k)}_{\mu,\nu}\right) \tag{S7}$$

with frequency $\omega^{(n)}_{\mu,\nu}=n\omega+(\lambda^\mu-\lambda^\nu)$, and amplitudes $a^{(n,k)}_{\mu,\nu}=|a^{(n,k)}_{\mu,\nu}|\exp\left(i\phi^{(n,k)}_{\mu,\nu}\right)=2\sum_p c^{\mu*}c^\nu\Phi^{\mu*}_{p+n,k}\Phi^\nu_{p,k}$. Note that when drawing a correspondence to the dynamical dipole matrix element of a probing operator V, the state $|k\rangle$ should be an eigenstate of the probing operator V.

B. Concatenated continuous driving

Concatenated continuous driving (CCD) is a dynamical decoupling technique with modulated driving fields, and it has been explored in the context of qubit coherence protection and noise decoupling [1, 3–14]. Although more complicated CCD schemes have been studied [3, 4], in this work, we focus on the simplest one where only one modulation is applied to the main driving field. We can classify the CCD schemes into two types: amplitude-modulated CCD and phase-modulated CCD.

Amplitude-modulated CCD - By applying an amplitude-modulated microwave with waveform $\omega_{\mu w}=\Omega\cos(\omega t)-2\epsilon_m\sin(\omega t)\cos(\omega_m t+\phi)$ to a qubit along the transverse x axis $\omega_{\mu w}\sigma_x$, the Hamiltonian in the lab frame can be written as

$$\mathcal{H}=\frac{\omega_0}{2}\sigma_z+\left(\Omega\cos(\omega t)-2\epsilon_m\sin(\omega t)\cos(\omega_m t+\phi)\right)\sigma_x \tag{S8}$$

where ω_0 is the level splitting of the qubit, Ω,ϵ_m are the driving and modulation strengths. We assume $\Omega,\epsilon_m\ll\omega_0$ and $\delta=\omega-\omega_0\ll\omega_0$ (as typically the power of AC fields is limited) such that the rotating wave approximation (RWA) is valid. In the first rotating frame defined by a unitary transformation $U=\exp\left(-i\frac{\omega t}{2}\sigma_z\right)$, and applying the RWA, the Hamiltonian becomes

$$\mathcal{H}_I=-\frac{\delta}{2}\sigma_z+\frac{\Omega}{2}\sigma_x+\epsilon_m\cos(\omega_m t+\phi)\sigma_y. \tag{S9}$$

Phase-modulated CCD - In the phase-modulated scheme, the driving waveform has a time-dependent phase and the Hamiltonian in the lab frame is

$$\mathcal{H} = \frac{\omega_0}{2}\sigma_z + \Omega\cos\left(\omega t + \frac{2\epsilon_m}{\omega_m}\cos(\omega_m t + \phi)\right)\sigma_x. \tag{S10}$$

The rotating frame transformation to simplify the analysis is defined by $U = \exp\left(-i\int_0^t H_0(t')dt'\right)$ with $\mathcal{H}_0(t) = (\omega/2)\sigma_z - (\epsilon_m\omega_m/\omega_m)\sin(\omega_m t+\phi)\sigma_z$ and then $U = \exp\left[-i\left(\frac{\omega t}{2}\sigma_z + \epsilon_m\frac{\cos(\omega_m t+\phi)}{\omega_m}\sigma_z\right)\right]$. Assuming that the RWA is valid, the Hamiltonian in the interaction picture is

$$\mathcal{H}_I = -\frac{\delta}{2}\sigma_z + \frac{\Omega}{2}\sigma_x + \epsilon_m\sin(\omega_m t+\phi)\sigma_z. \tag{S11}$$

Both amplitude-modulated CCD and phase-modulated CCD can implement similar Hamiltonians $\mathcal{H}_I$ comprising a static and an oscillating field. However, the amplitude modulation is applied by varying the second driving amplitude which is more affected by power fluctuations, while the phase modulation is applied by varying the driving phase $(2\epsilon_m/\omega_m)\cos(\omega_m t+\phi)$ and is robust against power fluctuations (although noise associated with imperfect resolution and faulty electronic elements are still possible). The phase-modulated CCD usually has better performance such as longer coherence time [6, 7, 14], and less power limitations, enabling larger ϵ_m.

C. Floquet solution to a driven qubit

We consider the Hamiltonian of the phase-modulated concatenated continuous driving in the interaction picture $\mathcal{H}_I = (\Omega/2)\sigma_x + \epsilon_m\sin(\omega_m t+\phi)\sigma_z$. Fourier decomposition of this Hamiltonian gives $\mathcal{H}_{I,0} = (\Omega/2)\sigma_x$, $H_{I,\pm1} = \mp[\epsilon_m e^{\mp i\phi}/(2i)]\sigma_z$. The Floquet matrix problem is

$$\begin{pmatrix}
\ddots & \vdots & \vdots & \vdots & \vdots & \vdots & \vdots & \\
\cdots & \omega_m & \frac{\Omega}{2} & -i\frac{\epsilon_m}{2}e^{i\phi} & 0 & 0 & 0 & \cdots \\
\cdots & \frac{\Omega}{2} & \omega_m & 0 & i\frac{\epsilon_m}{2}e^{i\phi} & 0 & 0 & \cdots \\
\cdots & i\frac{\epsilon_m}{2}e^{-i\phi} & 0 & 0 & \frac{\Omega}{2} & -i\frac{\epsilon_m}{2}ie^{i\phi} & 0 & \cdots \\
\cdots & 0 & -i\frac{\epsilon_m}{2}e^{-i\phi} & \frac{\Omega}{2} & 0 & 0 & i\frac{\epsilon_m}{2}e^{i\phi} & \cdots \\
\cdots & 0 & 0 & i\frac{\epsilon_m}{2}e^{-i\phi} & 0 & -\omega_m & \frac{\Omega}{2} & \cdots \\
\cdots & 0 & 0 & 0 & -i\frac{\epsilon_m}{2}e^{-i\phi} & \frac{\Omega}{2} & -\omega_m & \cdots \\
 & \vdots & \vdots & \vdots & \vdots & \vdots & \vdots & \ddots
\end{pmatrix}
\begin{pmatrix} \vdots \\ \Phi_{-1,0} \\ \Phi_{-1,1} \\ \Phi_{0,0} \\ \Phi_{0,1} \\ \Phi_{1,0} \\ \Phi_{1,1} \\ \vdots \end{pmatrix}
= \lambda
\begin{pmatrix} \vdots \\ \Phi_{-1,0} \\ \Phi_{-1,1} \\ \Phi_{0,0} \\ \Phi_{0,1} \\ \Phi_{1,0} \\ \Phi_{1,1} \\ \vdots \end{pmatrix}. \tag{S12}$$

Since we can always write the eigenstate $|\Phi(t)\rangle, |\Psi(t)\rangle$ in the basis of $V = \sigma_j$ ($|0_j\rangle$, $|1_j\rangle$), the evolution of the system can be written in a more general form as

$$|\Psi(t)\rangle = c^+e^{-i\lambda^+t}\sum_n\begin{pmatrix}\Phi^+_{n,0_j}\\ \Phi^+_{n,1_j}\end{pmatrix}e^{-in\omega_m t} + c^-e^{-i\lambda^-t}\sum_n\begin{pmatrix}\Phi^-_{n,0_j}\\ \Phi^-_{n,1_j}\end{pmatrix}e^{-in\omega_m t} = \sum_n\begin{pmatrix}c^+e^{-i\lambda^+t}\Phi^+_{n,0_j} + c^-e^{-i\lambda^-t}\Phi^-_{n,0_j}\\ c^+e^{-i\lambda^+t}\Phi^+_{n,1_j} + c^-e^{-i\lambda^-t}\Phi^+_{n,1_j}\end{pmatrix}e^{-in\omega_m t} \tag{S13}$$

where the coefficients $c^\pm$ are given by the initial condition $|\Psi(0)\rangle = \sum_\pm c^\pm|\Phi^\pm(0)\rangle$, and $0_j, 1_j$ denotes the component in the basis $|0_j\rangle, |1_j\rangle$ (for $\sigma_j = \sigma_x, \sigma_y, \sigma_z$, the basis $|0_j\rangle = |+\rangle, |+i\rangle, |0\rangle$ with $|+\rangle = (|0\rangle + |1\rangle)/\sqrt{2}$ and $|+i\rangle = (|0\rangle + i|1\rangle)/\sqrt{2}$).

For the Rabi measurements in this work, the qubit state is projected onto $|0_j\rangle$, the eigenstate of the probing operator $V \equiv \sigma_j$. The probability of being in the $|0_j\rangle$ state $P_{|0_j\rangle}(t)$ presents three classes of frequencies: $\{n\omega_m \pm (\lambda^+ - \lambda^-),\ n\omega_m\}$ where n is the integer denoting the band order:

$$\begin{aligned} P_{|0_j\rangle}(t) &= \sum_n e^{-in\omega_m t}(c^+e^{-i\lambda^+t}\Phi^+_{n,0_j} + c^-e^{-i\lambda^-t}\Phi^-_{n,0_j}) \times \sum_p e^{im\omega_m t}(c^{+*}e^{i\lambda^+t}\Phi^{+*}_{p,0_j} + c^{-*}e^{i\lambda^-t}\Phi^{-*}_{p,0_j}) \\ &= \sum_{n,p} e^{i(p-n)\omega_m t}\left(|c^+|^2\Phi^{+*}_{p,0_j}\Phi^+_{n,0_j} + |c^-|^2\Phi^{-*}_{p,0_j}\Phi^-_{n,0_j} + e^{-i(\lambda^+-\lambda^-)t}c^+c^{-*}\Phi^+_{n,0_j}\Phi^{-*}_{p,0_j} + e^{i(\lambda^+-\lambda^-)t}c^{+*}c^-\Phi^{+*}_{p,0_j}\Phi^-_{n,0_j}\right) \end{aligned} \tag{S14}$$

We can rewrite this expression as

$$P_{|0_j\rangle}(t) = \sum_{i,n} |a_i^{(n)}| \cos\left(\omega_i^{(n)} t + \phi_i^{(n)}\right) \tag{S15}$$

with $\omega_i^{(n)} = n\omega_m + i(\lambda^+ - \lambda^-)$, where $i = \pm 1, 0$ corresponding to sidebands and centerbands, respectively, $a_{\pm 1}^{(n)} = |a_{\pm 1}^{(n)}| \exp\left(i\phi_{\pm 1}^{(n)}\right) = 2\sum_p c^{\pm *} c^{\mp} \Phi^{\pm *}_{p+n,0_j} \Phi^{\mp}_{p,0_j}$, and $a_0^{(n)} = 2\sum_{\pm} |c^{\pm}|^2 \sum_p \Phi^{\pm *}_{p+n,0_j} \Phi^{\pm}_{p,0_j}$

II. CORRESPONDENCE BETWEEN RABI AMPLITUDES AND SUSCEPTIBILITY

In Ref. [15], Floquet bands were probed through the susceptibility χ, as typically done in light scattering experiments. Here we instead reveal the Floquet bands through the Rabi amplitudes of the coherent evolution of a driven qubit [1]. Before proceeding to derive the selection rules in the Rabi measurement, we first establish the correspondence between Rabi amplitudes and susceptibility χ.

Susceptibility χ - In Ref. [15], the Floquet band structure of a periodically driven qubit is probed through a bichromatic probe field ($\omega_{p,1}$ and $\omega_{p,2} = \omega_{p,1} + n\omega_m$) where the intensity change of the second frequency component $\Delta I(\omega_{p,2}) = [-i\chi_n(\omega_{p,1}) \langle \hat{a}^\dagger_{\omega_{p,2}} \hat{a}_{\omega_{p,1}} \rangle + c.c.]$ is used to identify the symmetry-protected selection rules. There, the susceptibility $\chi_n(\omega_{p,1})$ was defined as

$$\chi_n(\omega_{p,1}) = i\lambda^2 \sum_{\mu,\nu,m} \frac{V^{(-n-m)}_{\nu,\mu} V^{(m)}_{\mu,\nu} (p_\nu - p_\mu)}{\lambda^\mu - \lambda^\nu + m\omega_m - \omega_{p,1} - i\gamma^{(m)}_{\nu,\mu}} \tag{S16}$$

where γ is a phenomenological dephasing factor, and the probabilities $\{p_\mu\}$ are associated with the assumption of a long time stationary state $\rho(t) = \sum_\mu p_\mu |\Phi^\mu(t)\rangle \langle \Phi^\mu(t)|$ [15]. The symmetry-protected dark states (spDS) and dark bands (spDB) are induced by a vanishing dynamical dipole matrix element $V^{(n)}_{\mu,\nu} = 0$ and susceptibility $\chi_n(\omega_{p.1}) = 0$, respectively, and the symmetry-induced transparency (siT) is induced by the destructive interference of two nonzero dynamical dipole matrix elements $V^{(n)}_{\mu,\nu} \neq 0$.

N-level system - In this work, we discuss the selection rules in the context of a coherent state evolution, and we find that the spDSs, spDBs, and siT also appear in the coherent state evolution under similar conditions. According to Floquet theory, the state evolution of a periodically-driven quantum system is $|\Psi(t)\rangle = \sum_\mu c^\mu e^{-i\lambda^\mu t} |\Phi^\mu(t)\rangle$ where $|\Phi^\mu(t)\rangle = \sum_{n=-\infty}^{+\infty} e^{-in\omega t} |\Phi^\mu_n\rangle$, and c^μ is determined by the initial condition $|\Psi(0)\rangle = \sum_\mu c^\mu |\Phi(0)\rangle$. Assuming the probing operator can be written as $V = \sum_k \mathcal{V}_k |k\rangle\langle k|$, the dynamical dipole matrix element $V^{(n)}_{\mu,\nu}$ can be calculated as

$$V^{(n)}_{\mu,\nu} = \frac{1}{T} \int_0^T \langle \Phi^\mu(t)|V|\Phi^\nu(t)\rangle e^{-in\omega t} dt, \tag{S17}$$

Using $|\Phi^\mu(t)\rangle = \sum_n |\Phi^\mu_n\rangle e^{-in\omega t}$ and $V = \sum_k \mathcal{V}_k |k\rangle\langle k|$, we have

$$V^{(n)}_{\mu,\nu} = \sum_k \mathcal{V}_k \sum_p \langle \Phi^\mu_p | k\rangle \langle k | \Phi^\nu_{p-n}\rangle = \sum_{p,k} \mathcal{V}_k \Phi^{\mu *}_{p,k} \Phi^\nu_{p-n,k}. \tag{S18}$$

where $\Phi^{\mu *}_{p,k} = \langle \Phi^\mu_p | k\rangle, \Phi^\nu_{p-n,k} = \langle k | \Phi^\nu_{p-n}\rangle$. We define a "weighted Rabi oscillation" for the N-level system as

$$P(t) = \sum_k \frac{\mathcal{V}_k}{\mathcal{V}} P_{|k\rangle}(t) \tag{S19}$$

where $\mathcal{V} = \sum_k |\mathcal{V}_k|$ is the normalization factor and $P_{|k\rangle}(t) = |\langle k|\Psi(t)\rangle|^2$ is the measured population on $|k\rangle$. Then we have

$$\mathcal{V} P(t) = \langle V \rangle = \langle \Psi(t)| V |\Psi(t)\rangle \tag{S20}$$

with $|\Psi(t)\rangle = \sum_\mu c^\mu |\Phi^\mu(t)\rangle e^{-i\lambda^\mu t} = \sum_{\mu,n} c^\mu |\Phi^\mu_n\rangle e^{-in\omega t} e^{-i\lambda^\mu t}$, we obtain

$$\langle V \rangle = \sum_{\mu,\nu,n} c^{\mu *} c^\nu e^{i(\lambda^\mu - \lambda^\nu)t} e^{in\omega t} V^{(n)}_{\mu,\nu} \tag{S21}$$

This weighted Rabi oscillation can then be decomposed into a series of frequency components as

$$P(t) = \frac{\langle V \rangle}{\mathcal{V}} = \sum_{\mu,\nu,n} |a^{(n)}_{\mu,\nu}| \cos\left(\omega^{(n)}_{\mu,\nu} t + \phi^{(n)}_{\mu,\nu}\right), \tag{S22}$$

with frequencies $\omega^{(n)}_{\mu,\nu} = n\omega + (\lambda^\mu - \lambda^\nu)$, and amplitudes $a^{(n)}_{\mu,\nu} = |a^{(n)}_{\mu,\nu}| \exp\left(i\phi^{(n)}_{\mu,\nu}\right) = 2\sum_{p,k} c^{\mu *} c^\nu (\mathcal{V}_k/\mathcal{V}) \Phi^{\mu *}_{p+n,k} \Phi^\nu_{p,k}$. When $\mu = \nu$, the observed signal arises from the coherent interference of all centerbands, resulting in amplitudes $a^{(n)}_0 = |a^{(n)}_0| \exp\left(i\phi^{(n)}_0\right) = 2\sum_{\mu,p,k} |c^\mu|^2 (\mathcal{V}_k/\mathcal{V}) \Phi^{\mu *}_{p+n,k} \Phi^\mu_{p,k}$. Interference of sidebands can happen at energy degeneracy points, such as $\lambda^\mu = \lambda^\nu$. For N-level systems, the frequency modes of the Rabi oscillation $P(t)$ are comprised of a series of equidistant manifolds, with one centerband $n\omega$ and $N(N-1)$ sidebands $n\omega + (\lambda^\mu - \lambda^\nu)$ within each manifold.

As derived above, we obtain the correspondence between the weighted Rabi amplitudes and the dynamical dipole matrix element

$$a^{(n)}_{\mu,\nu\neq\mu} = 2c^{\mu *} c^\nu \frac{V^{(n)}_{\mu,\nu}}{\mathcal{V}}, \tag{S23}$$

$$a^{(n)}_0 = 2\sum_\mu |c^\mu|^2 \frac{V^{(n)}_{\mu,\mu}}{\mathcal{V}}. \tag{S24}$$

The off-diagonal terms of the dynamical dipole transition element $2c^{\mu *} c^\nu V^{(n)}_{\mu,\nu\neq\mu}/\mathcal{V}$ can be exactly mapped to the sideband amplitudes $a^{(n)}_{\mu,\nu\neq\mu}$, and the weighted summation of the diagonal terms $2\sum_\mu |c^\mu|^2 V^{(n)}_{\mu,\mu}/\mathcal{V}$ can be mapped to the centerbands amplitude $a^{(n)}_0$.

Quantum mode control - Since we have phase control over the applied microwave, we can selectively observe centerbands or sidebands by tuning the coefficients c^μ through the initial condition (*quantum mode control*) as discussed in both the main text and in Ref. [1]. As a result, all elements of the dynamical dipole matrix $V^{(n)}_{\mu,\nu}$ can be individually probed through *quantum mode control*. We clarify that symmetry-protected selection rules discussed in this work determine the selection rule of $V^{(n)}_{\mu,\nu}$, while *quantum mode control* determines via c^μ which mode amplitudes are observed, by tuning the initial state with respect to the Floquet eigenstates.

2-level system - According to Floquet theory, the state evolution of a driven qubit is $|\Psi(t)\rangle = \sum_\pm c^\pm e^{-i\lambda^\pm t} |\Phi^\pm(t)\rangle$ where $|\Phi^\pm(t)\rangle = \sum_{n=-\infty}^{+\infty} e^{-in\omega_m t} |\Phi^\pm_n\rangle$. For the two-level qubit, the probing operators $\sigma_x, \sigma_z, \sigma_y$ can be written as $\sigma_x = |+\rangle\langle+| - |-\rangle\langle-|, \sigma_y = |+i\rangle\langle+i| - |-i\rangle\langle-i|, \sigma_x = |0\rangle\langle 0| - |1\rangle\langle 1|$, thus the dynamical dipole matrix element $V^{(n)}_{\mu,\nu}$ can be simply calculated as

$$V^{(n)}_{\mu,\nu} = \frac{1}{T}\int_0^T \langle \Phi^\mu(t)|V|\Phi^\nu(t)\rangle e^{-in\omega t} dt = \sum_p \left(\Phi^{\mu *}_{p,0_j} \Phi^\nu_{p-n,0_j} - \Phi^{\mu *}_{p,1_j} \Phi^\nu_{p-n,1_j}\right) \tag{S25}$$

where $\mu, \nu \in \{+,-\}$ corresponding to the two Floquet eigenstates, and $0_j, 1_j$ denote the projection on the two eigenstates of the probing operator $V = \sigma_j$. Since $P_{|0_j\rangle}(t) + P_{|1_j\rangle}(t) = 1$, the measurement of the weighted Rabi is $(1/2)\left[P_{|0_j\rangle}(t) - P_{|1_j\rangle}(t)\right] = P_{|0_j\rangle}(t) - 1/2$, we can measure the typical qubit Rabi oscillation $P_{|0_j\rangle}$ instead of the equivalent population difference between $|0_j\rangle$ and $|1_j\rangle$ (except for the zero frequency component where the equivalence is no longer satisfied). The Rabi amplitudes $P_{|0_j\rangle}$ in Eq. (S22) can be expressed in terms of the dynamical dipole matrix elements as listed in Table. S1.

TABLE S1. Correspondence between the Rabi amplitudes $a^{(n)}_i$ and dipole matrix element $V^{(n)}_{\mu,\nu}$ for a TLS. Note that $\Phi^\mu_{p,0_j} = \langle 0_j | \Phi^\mu_p \rangle$, and listed cases do not include $i = n = 0$ [1].

Bands$_{\{i,n\}}$	Rabi amplitudes $a^{(n)}_{\mu,\nu}$	Expressed in $V^{(n)}_{\mu,\nu}$
{0,n}	$2\sum_\pm \lvert c^\pm\rvert^2 \sum_k \Phi^{\pm *}_{k+n,0_j} \Phi^\pm_{k,0_j}$	$\lvert c^+\rvert^2 V^{(n)}_{+,+} + \lvert c^-\rvert^2 V^{(n)}_{-,-}$
{-1,n}	$2\sum_k c^+ c^{-*} \Phi^+_{k,0_j} \Phi^{-*}_{k+n,0_j}$	$c^+ c^{-*} V^{(n)}_{-,+}$
{+1,n}	$2\sum_k c^{+*} c^- \Phi^{+*}_{k+n,0_j} \Phi^-_{k,0_j}$	$c^{+*} c^- V^{(n)}_{+,-}$

III. OBSERVATION OF SYMMETRIES IN A TWO-LEVEL SYSTEM

We apply the phase-modulated CCD technique to engineer the interaction picture Hamiltonian

$$\mathcal{H}_I = \frac{\Omega}{2}\sigma_x + \epsilon_m \sin(\omega_m t + \phi)\sigma_z. \tag{S26}$$

The time period of such a Hamiltonian is $T = 2\pi/\omega_m$.

A. Parity (2-fold rotation) symmetry σ_x

The first symmetry associated with the Hamiltonian $\mathcal{H}_I$ in Eq. (S26) is a 2-fold rotation or, equivalently, a parity symmetry given by the operator $\hat{R} = \sigma_x$, satisfying $\hat{R}\mathcal{H}_I(t + T/2)\hat{R}^\dagger = \mathcal{H}_I(t)$. Such a symmetry gives rise to the relation between eigenstates $|\Phi^\mu(t)\rangle = \pi_\mu^{(R)}\hat{R}\,|\Phi^\mu(t + T/2)\rangle = e^{i\pi m_\mu}\hat{R}\,|\Phi^\mu(t + T/2)\rangle$ with $\mu \in \{-, +\}$ and $m_\mu \in \{0, 1\}$ [15]. In Fig. S1 we numerically calculate and plot the Floquet eigenstates $|\Phi^\pm(t)\rangle$ under the resonance condition $\Omega = \omega_m = (2\pi)3\text{MHz}$, for a modulation strength $2\epsilon_m/\omega_m = 2.75$ and phase $\phi = 0$. Under such condition, $\pi_\pm^{(R)} = \pm 1$, as validated in the comparison between Figs. S1(a,d) and Figs. S1(c,f).

The values of $\pi_\mu^{(R)}$ depend on the modulation parameters we choose (and also on how the band range is defined, as discussed in Ref. [1]). In Figs. S2(c,f) we plot the two values of $\pi_\pm^{(R)}$ as a function of $2\epsilon_m/\omega_m$. Note that $\pi_\pm^{(R)} = \pm 1$, and their value switches sign (or in other words π_+ switches with π_-) when the eigenvalues cross the degeneracy point (under the assumption that $\lambda^- < \lambda^+$ and defining the band as, $\lambda^\pm \in (-\omega_m/2, \omega_m/2]$). Due to the parity symmetry (2-fold rotational symmetry), the relation $\pi_+^{(R)}\pi_-^{(R)} = -1$ is satisfied, which is used in the following derivations of selection rules.

We now derive the selection rule by evaluating the value of the dynamical dipole matrix element, which is

$$V_{\mu,\nu}^{(n)} = \frac{1}{T}\int_0^T \langle\Phi^\mu(t)|V|\Phi^\nu(t)\rangle e^{-in\omega_m t}dt = \frac{1}{T}\int_0^{T/2} \langle\Phi^\mu(t)|V|\Phi^\nu(t)\rangle e^{-in\omega_m t}dt \times \left[1 + \pi_\mu^{(R)}\pi_\nu^{(R)*}e^{-i\pi n}\alpha_V\right]$$

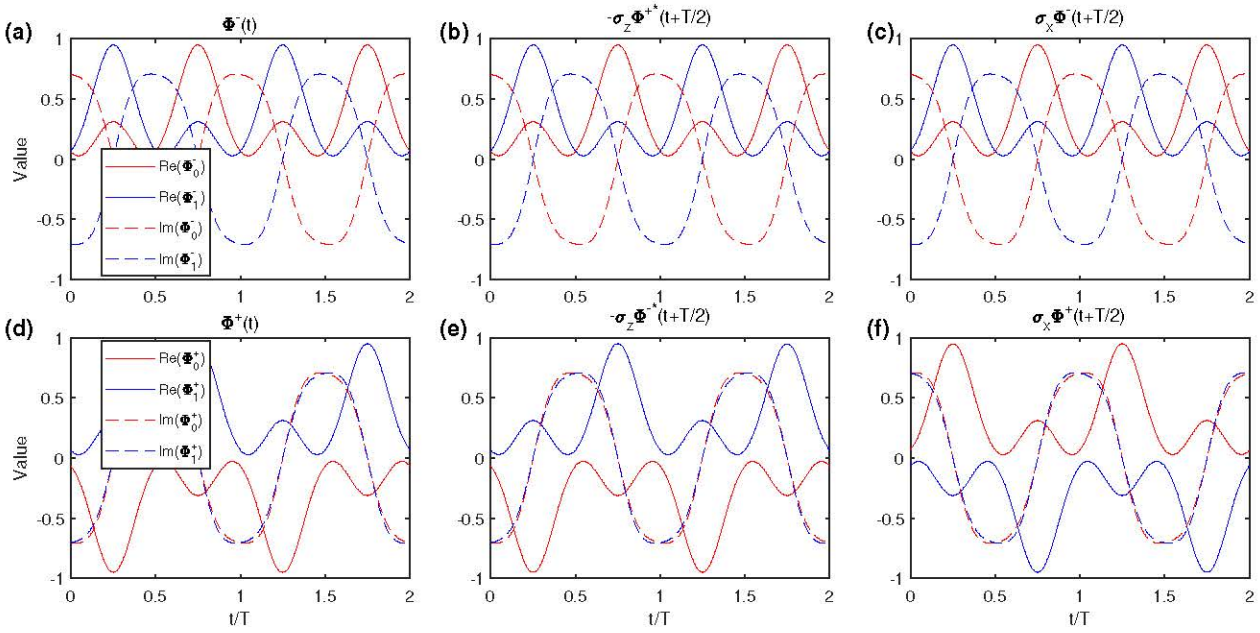

FIG. S1. Symmetry of Floquet eigenstates $|\Phi^\pm(t)\rangle$. Floquet simulation is applied to calculate the time-dependent Floquet eigenstates $|\Phi^\pm(t)\rangle$ under the condition $2\epsilon_m/\omega_m = 2.75$, $\phi = 0$, and $\omega_m = \Omega = (2\pi)3\text{MHz}$. (a) $\Phi^-(t)$ plotted in the first two time periods. Since $\Phi^-(t)$ is a 2×1 normalized complex vector, we plot the real (solid line) and imaginary (dashed lines) parts of each component (red and blue colors). The basis used here is the σ_z basis. Same rules apply for the other plots. (b) $-\sigma_z\Phi^{+*}(t + T/2)$. (c) $\sigma_x\Phi^-(t + T/2)$. (d) $\Phi^+(t)$. (e) $-\sigma_z\Phi^{-*}(t + T/2)$. (f) $\sigma_x\Phi^+(t + T/2)$.

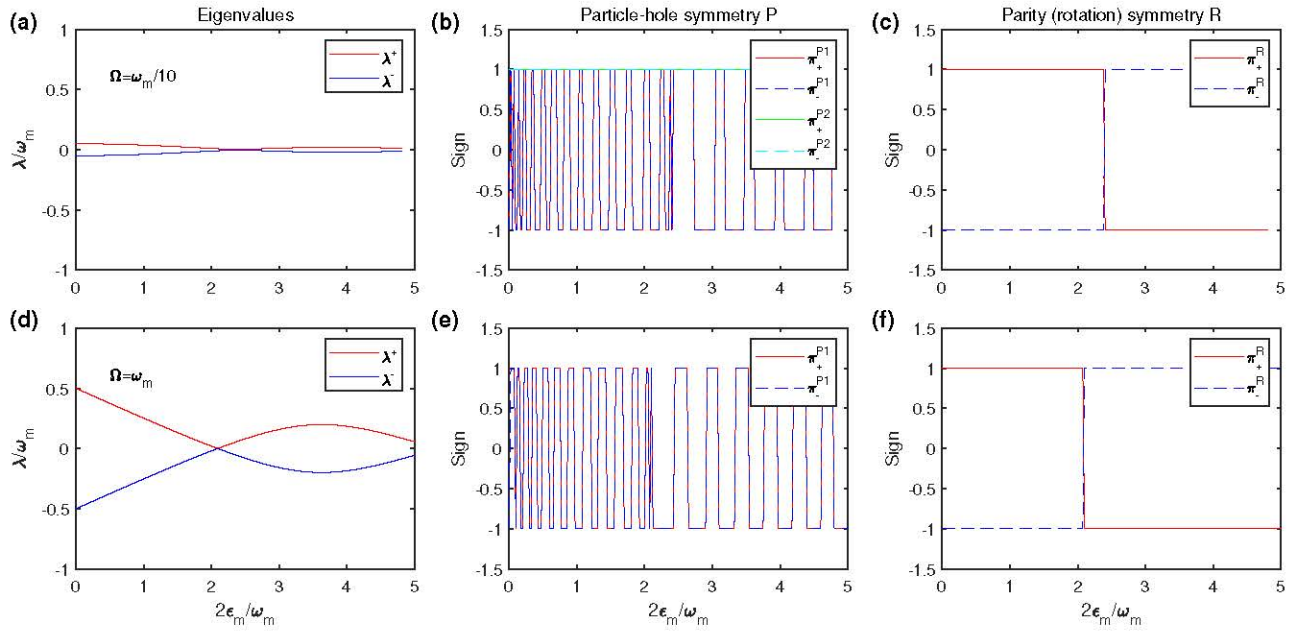

FIG. S2. Floquet eigenenergies and π_μ. (a) Floquet eigenenergies $\lambda^{\pm}$ under the condition $\phi = 0$, $\omega_m = 10\Omega = (2\pi)15$MHz. Note that $\lambda^{\pm}$ is defined in the range $(-\omega_m/2, \omega_m/2]$ and $\lambda^- \leq \lambda^+$. (b) The values of $\pi_{\pm}^{(P_1)}$, $\pi_{\pm}^{(P_2)}$ corresponding to the two particle-hole symmetries $\hat{P}_1 = \sigma_z$, $\hat{P}_2 = I$ under the condition in (a). (c) The values of $\pi_{\pm}^{(R)}$ corresponding to the parity symmetry $\hat{R} = \sigma_x$ under the condition in (a). (d) Floquet eigenenergies $\lambda^{\pm}$ under the condition $\phi = 0$, $\omega_m = \Omega = (2\pi)3$MHz. (e) The values of $\pi_{\pm}^{(P_1)}$ corresponding to the particle-hole symmetry $\hat{P}_1 = \sigma_z$ under the condition in (d). (f) The values of $\pi_{\pm}^{(R)}$ corresponding to the parity symmetry $\hat{R} = \sigma_x$ under the condition in (d).

where the value of α_V is given by the relation $\hat{R}V\hat{R}^\dagger = \alpha_V V$. When the observation operator is $V = \sigma_y, \sigma_z$, such that $\alpha_V = -1$, Mollow centerbands with odd (n) orders are visible, while the even orders vanish. The opposite is true for the sidebands. When the observation operator is $V = \sigma_x$, such that $\alpha_V = 1$, Mollow centerbands with even (n) orders are visible while the odd orders vanish. The sidebands show the opposite behavior: the odd orders are visible as $\pi_+^{(R)}\pi_-^{(R)} = -1$, while the even orders disappear. These predictions are observed in both simulations (Fig. S4) and in experiments reported in the main text. Here we also show the complete data for the experiments in Fig. S3) as well as the experimental raw data (Fig. S5) before Fourier transform that would yield the spectrum in Fig. S3. The Rabi oscillations under different modulation strengths $2\epsilon_m/\omega_m$ are shifted vertically to avoid overlap.

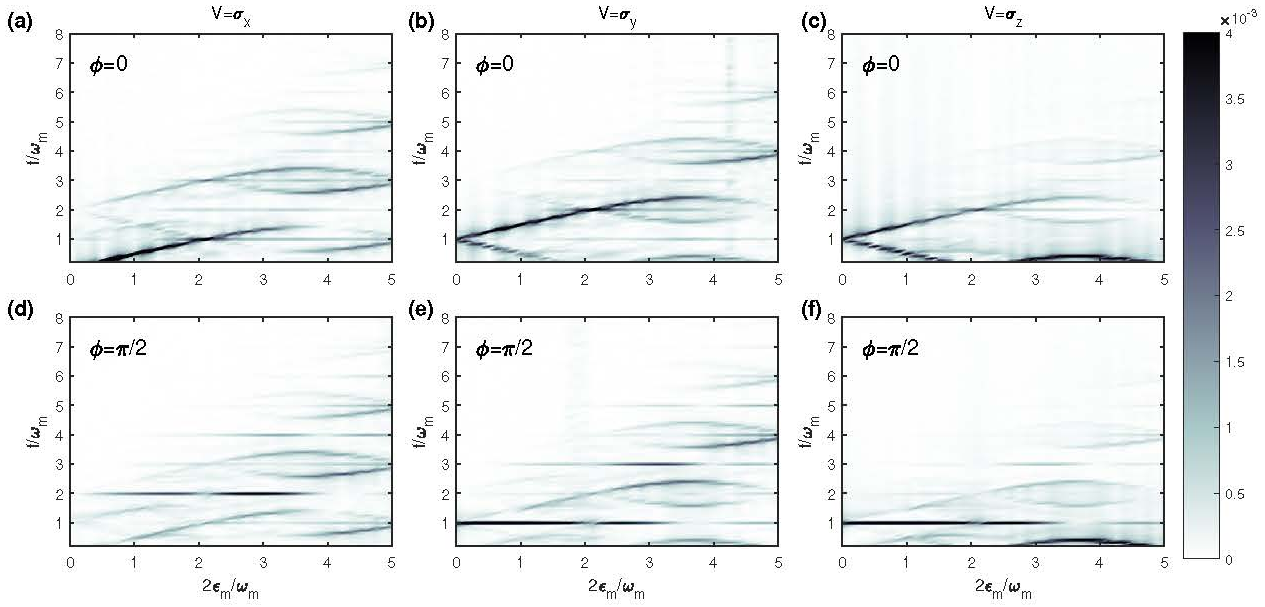

FIG. S3. Experimental observation of spDBs, spDSs, and destructive interference between centerbands. The Hamiltonian $\mathcal{H}_I$ in Eq. (S26) is engineered by the phase-modulated CCD technique with parameters $\Omega = \omega_m = (2\pi)3\text{MHz}$, $\phi = 0, \pi/2$ corresponding to (a-c,b-d). Rabi oscillations of an initial state $|0\rangle$ from $t = 0$ to $t = 4\mu s$ are measured with 401 sampling points and their Fourier spectrum are plotted as intensity map. (a,d) Fourier spectrum of Rabi measurement on $|+\rangle$ ($V = \sigma_x$) under different modulation strength $2\epsilon_m/\omega_m$. (b,e) Fourier spectrum of Rabi measurement on $|+i\rangle$ ($V = \sigma_y$) under different modulation strength $2\epsilon_m/\omega_m$. (c,f) Fourier spectrum of Rabi measurement on $|0\rangle$ ($V = \sigma_z$) under different modulation strength $2\epsilon_m/\omega_m$. Please check the complete raw data in Fig. S5.

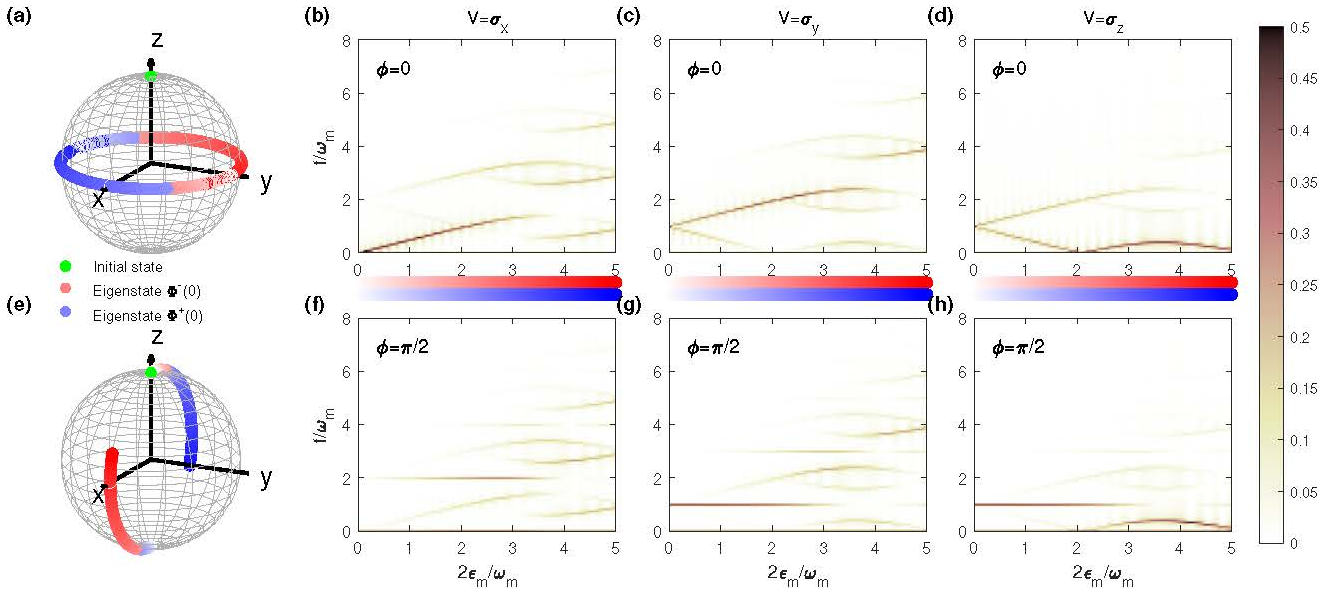

FIG. S4. Simulation of spDBs, spDSs, and destructive interference between centerbands under the Hamiltonian $\mathcal{H}_I$ in Eq. (S26). (a,e) Floquet eigenstates $|\Phi^{\pm}(0)\rangle$ visualized on a Bloch sphere. Floquet eigenstates are calculated with the Hamiltonian in Eq. (S26). Modulation strength $2\epsilon_m/\omega_m$ is swept from 0 to 5 with darker colors, and other parameters are $\Omega = \omega_m = (2\pi)3\text{MHz}$, $\phi = 0, \pi/2$ corresponding to (a-d), (e-h) respectively. (b,f) Fourier spectrum of Rabi measurement on $|+\rangle$ ($V = \sigma_x$) under different modulation strength $2\epsilon_m/\omega_m$. Rabi oscillations of an initial state $|0\rangle$ from $t = 0$ to $t = 4\mu s$ are simulated and their Fourier spectrum are plotted as intensity map. (c,g) Fourier spectrum of Rabi measurement on $|+i\rangle$ ($V = \sigma_y$) under different modulation strength $2\epsilon_m/\omega_m$. Other parameters are the same as in (b,f). (d,h) Fourier spectrum of Rabi measurement on $|0\rangle$ ($V = \sigma_z$) under different modulation strength $2\epsilon_m/\omega_m$. Other parameters are the same as in (b,f).

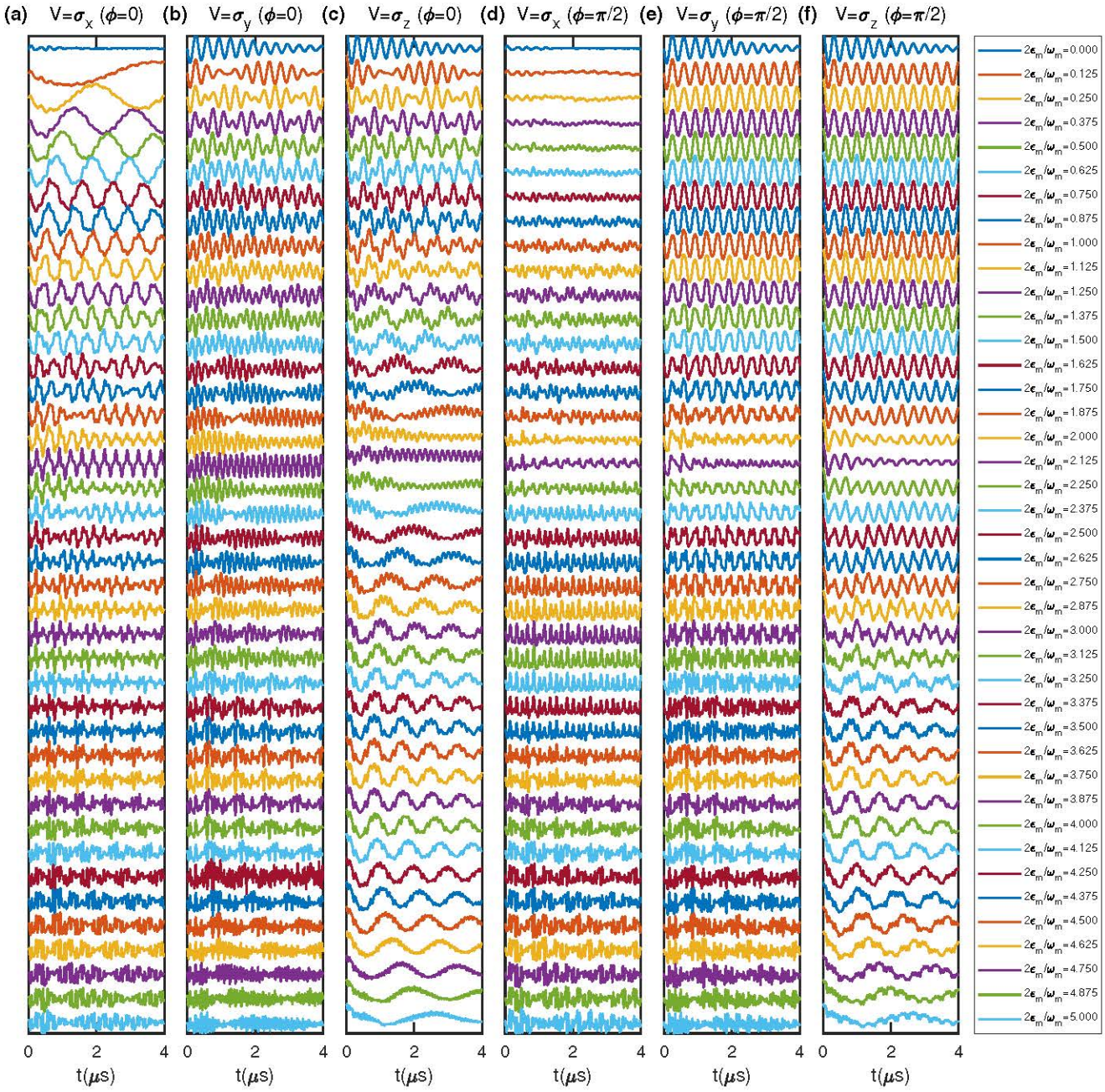

FIG. S5. Raw data of Fig. S3. (a-f) correspond to Figs. S3(a-f), respectively. Legend shows the corresponding modulation strength $2\epsilon_m/\omega_m$. We shift different curves manually to make them easier to read.

B. Particle-hole symmetry σ_z

The second symmetry is a particle-hole symmetry $\hat{P}_1 = \sigma_z$, which yields $\hat{P}_1 \mathcal{H}_I(t+T/2)\hat{P}_1^{\dagger} = -\mathcal{H}_I(t)$. Given an eigenstate $|\Phi^{\mu}(t)\rangle$ corresponding to the eigenenergy λ^{μ}, its counterpart $\hat{P}_1 |\Phi^{\mu *}(t+T/2)\rangle$ is also an eigenstate of the system with eigenenergy $-\lambda^{\mu}$. For our qubit system with two nontrivial eigensolutions (two eigenvalues are defined within the first "Brillouin zone" $(-\omega_m/2, \omega_m/2]$), such a relation yields $|\Phi^{-\mu}(t)\rangle = \pi_{\mu}^{(P_1)} \hat{P}_1 |\Phi^{\mu *}(t+T/2)\rangle$ where $\pi_{\mu}^{(P_1)}$ is gauge-dependent [15]. Here we have $\pi_{\mu}^{(P_1)} \in \{1, -1\}$ as validated by Floquet simulations – compare Figs. S1(a,d) and Figs. S1(b,e).

From the equality $|\Phi^{\mu}(t)\rangle = \pi_{\mu'}^{(P_1)} \hat{P}_1 \left|\Phi^{\mu' *}(t+T/2)\right\rangle = \pi_{\mu'}^{(P_1)} \hat{P}_1 \pi_{\mu}^{(P_1)*} \hat{P}_1^{*} |\Phi^{\mu}(t+T)\rangle = \pi_{\mu}^{(P_1)} \pi_{\mu'}^{(P_1)*} |\Phi^{\mu}(t)\rangle$, we obtain that $\pi_{\mu}^{(P_1)} \pi_{\mu'}^{(P_1)*} = 1$, though the specific values of $\pi_{\mu}^{(P_1)}$ depend on the parameter $2\epsilon_m/\omega_m$. In Figs. S2(b,e), we plot the values of $\pi_{\mu}^{(P_1)}$ for $\Omega = \omega_m/10$, $\Omega = \omega_m$, as a function of the modulation strength $2\epsilon_m/\omega_m$. We note that the condition $\pi_{\mu}^{(P_1)} \pi_{\mu'}^{(P_1)} = 1$ is always satisfied although the value of $\pi_{\mu}^{(P_1)}$ depends on the modulation parameter.

The dynamical dipole matrix element can be calculated as

$$\begin{aligned} V_{\mu,\nu}^{(n)} =& \frac{1}{T}\int_0^T \langle \Phi^{\mu}(t)|V|\Phi^{\nu}(t)\rangle e^{-in\omega_m t} dt = \frac{1}{T}\int_0^T \langle \Phi^{\mu' *}(t+T/2)|\pi_{\mu'}^{(P_1)*} \hat{P}_1^{\dagger} V \hat{P}_1 \pi_{\nu'}^{(P_1)} |\Phi^{\nu' *}(t+T/2)\rangle e^{-in\omega_m t} dt \\ =& \alpha_V^{(P_1)} e^{i\pi n} V_{\mu',\nu'}^{(-n)*} = \alpha_V^{(P_1)} e^{i\pi n} V_{\nu',\mu'}^{(n)} \end{aligned} \tag{S27}$$

where $\alpha_V^{(P_1)}$ is given by the relation $\hat{P}_1^{\dagger} V \hat{P}_1 = \alpha_V^{(P_1)} V^*$. Since the particle-hole symmetry operator $\hat{P}_1 = \sigma_z$ maps the Floquet eigenstate to its counterpart, rather than to itself as for the parity symmetry, we have to consider the following two situations:

1. When $\mu \neq \nu$, the symmetry gives rise to selection rules for the Mollow sidebands with $(\mu, \nu) = (\nu', \mu')$ such that $V_{\mu,\nu}^{(n)} = \alpha_V^{(P_1)} e^{i\pi n} V_{\mu,\nu}^{(n)}$.

   - When the observation operator is $V = \sigma_z$, $\alpha_V^{(P_1)} = 1$, only even-order Mollow sidebands are visible.
   - When the observation operator is $V = \sigma_x$, $\alpha_V^{(P_1)} = -1$, only odd-order Mollow sidebands are visible.

   This is consistent with the prediction from parity symmetry.

2. When $\mu = \nu$, the symmetry gives rise to vanishing centerbands when $|c^+|^2 = |c^-|^2 = 1/2$ (that is, when the initial state is an equal superposition of two Floquet eigenstates) and $\alpha_V^{(P_1)} e^{i\pi n} = -1$.

   - When the observation operator is $V = \sigma_z$, $\alpha_V^{(P_1)} = 1$, only even-order Mollow sidebands are visible, since $V_{+,+}^{(n)} = -V_{-,-}^{(n)}$ for $\alpha_V e^{-i\pi n} = -1$ with odd n.
   - When the observation operator is $V = \sigma_x$, $\alpha_V^{(P_1)} = -1$, only odd-order Mollow sidebands are visible.
   - Combining the selection rules for both particle-hole symmetry and parity symmetry, no centerband is visible for both observation operators.

We confirm this last prediction by observing that centerbands disappear for $\phi = 0$ (yielding $|c^{\pm}|^2 = 1/2$) in both experiment (Fig. S3) and simulation (Fig. S4), while they reappear for $\phi = \pi/2$ since then $|c^{\pm}|^2 \neq 1/2$. To clarify the relationship between the phase and the initial state coefficients, we plot the Floquet eigenstates on the Bloch sphere in Figs. S4(a,e). Under the modulation phase $\phi = 0$, the Floquet eigenstate is always in the $x-y$ plane, such that $|c^{\pm}|^2 = 1/2$ is always satisfied. Under the modulation phase $\phi = \pi/2$, the Floquet eigenstate is in the $x-z$ plane such that $|c^{\pm}|^2 \neq 1/2$, except at modulation strength $2\epsilon_m/\omega_m \approx 4$ where $|c^{\pm}|^2 = 1/2$ is accidentally satisfied.

Note that $\hat{P}\hat{P}^* = I$ is required for particle-hole symmetry, thus when considering the amplitude-modulated CCD scheme, where the periodically driving fields are along the y direction, a frame transformation to align the driving fields to the z direction is needed before applying a particle-hole symmetry analysis.

C. Symmetry Breaking

To demonstrate that the selection rules arise from the symmetries of the Hamiltonian, we spoil such symmetries by introducing additional terms. The complete experimental data under the resonance condition $\Omega = \omega_m = (2\pi)3\text{MHz}$ under an engineered symmetry breaking Hamiltonian is plotted in Fig. S6, where the appearance of more forbidden bands (in comparison to Fig. S3) clearly signals the symmetry breaking. Corresponding simulations are plotted in Fig. S7. See also section VI for experimental limitations that might induce weak breaking of the symmetries.

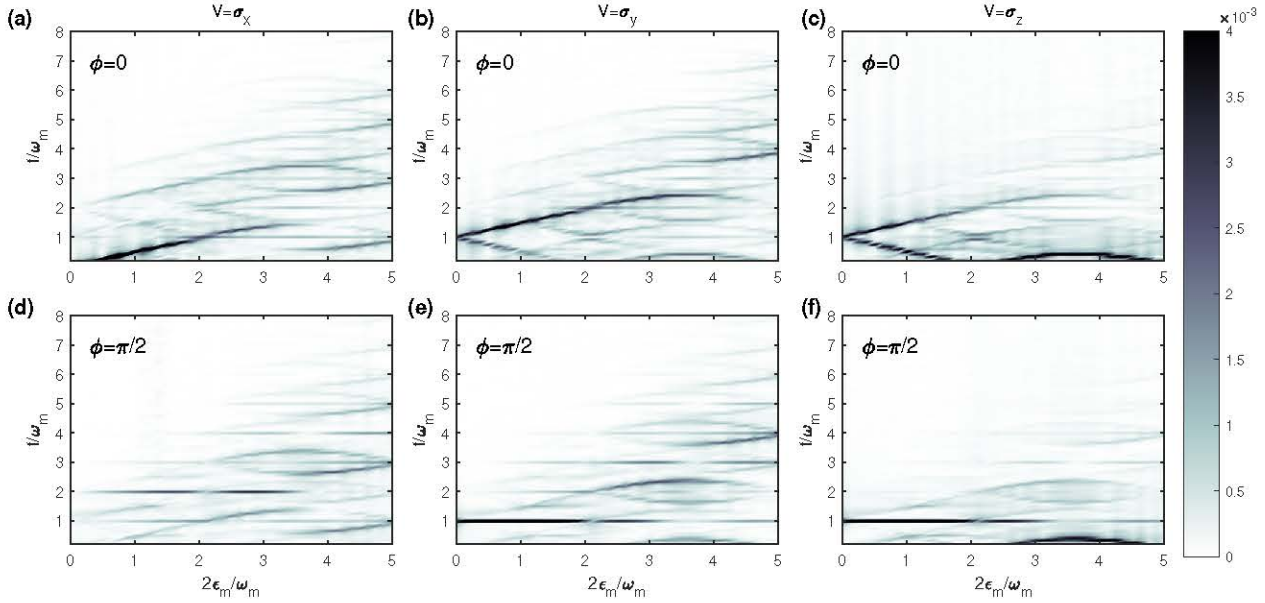

FIG. S6. Experimental observation of symmetry breaking. Same experiment conditions are used as in Fig. S3 except for the engineered Hamiltonian $\mathcal{H}'_I = (\Omega/2)\sigma_x + \epsilon_m \sin(\omega_m t + \phi) + 0.2\epsilon_m \sin(2\omega_m t + \phi)$ where the third term breaks both the parity symmetry and particle-hole symmetry.

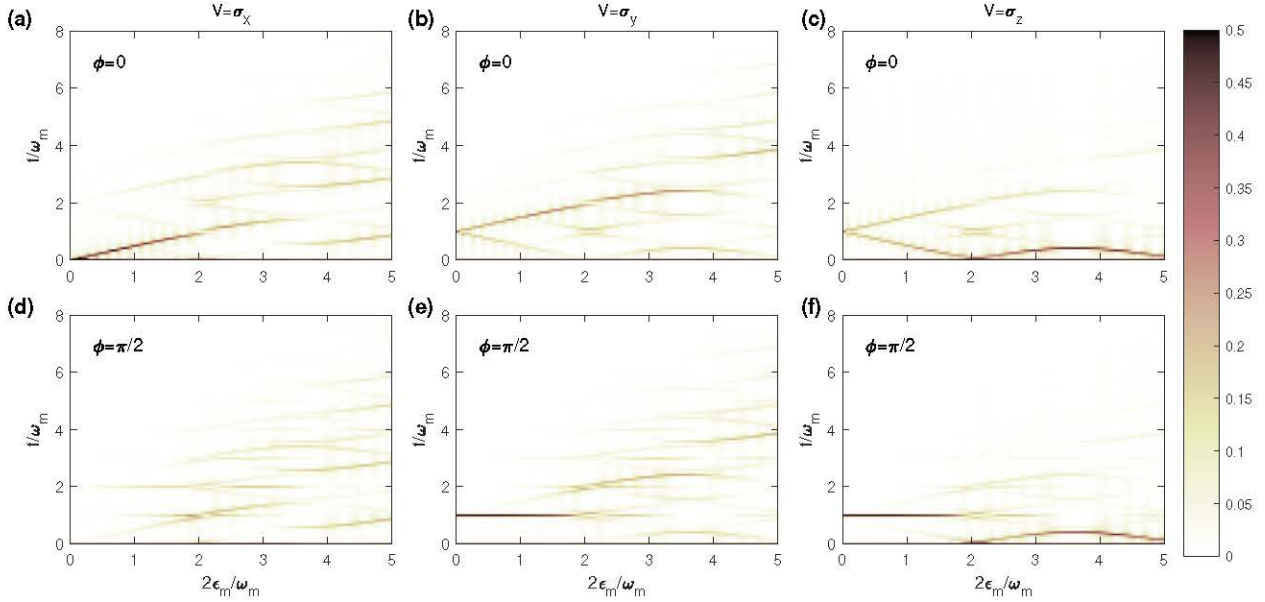

FIG. S7. Simulation of symmetry breaking. Same parameters are used as in Fig. S4 except for the Hamiltonian $\mathcal{H}' = (\Omega/2)\sigma_x + \epsilon_m \sin(\omega_m t + \phi)\sigma_z + 0.2\epsilon_m \sin(2\omega_m t + \phi)\sigma_z$ where the third term breaks both the parity symmetry and particle-hole symmetry.

IV. SYMMETRY-INDUCED TRANSPARENCY (SIT OR CDT)

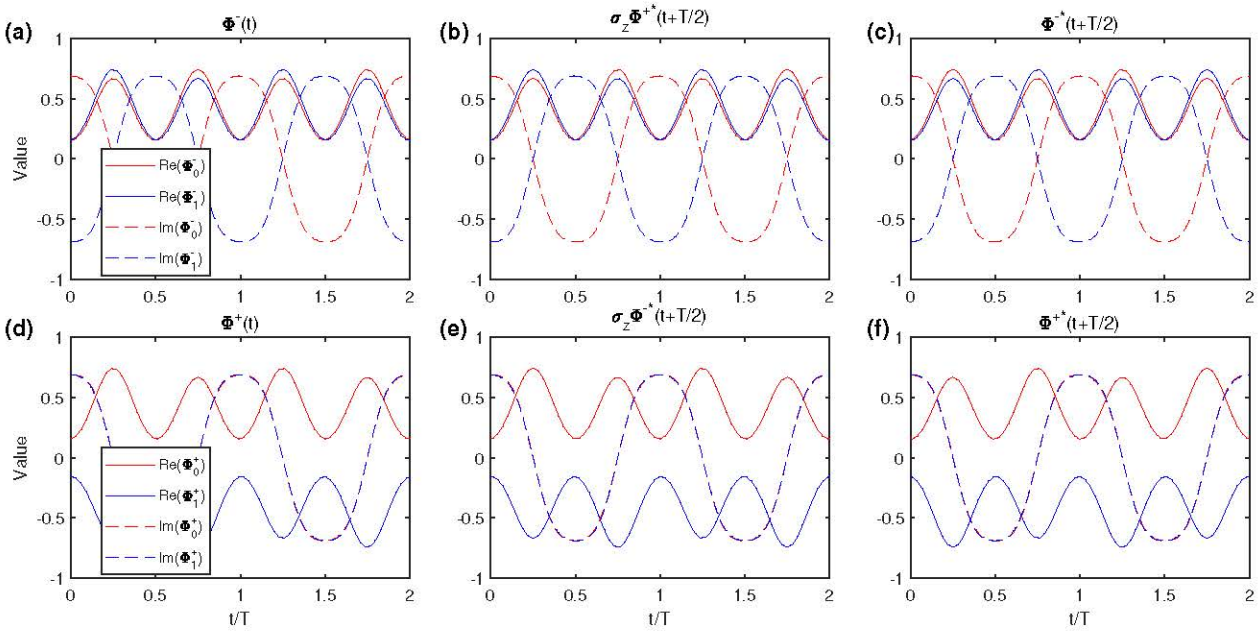

FIG. S8. Symmetry of Floquet eigenstates $|\Phi^{\pm}(t)\rangle$. Floquet simulation is applied to calculate the time-dependent Floquet eigenstates $|\Phi^{\pm}(t)\rangle$ under the condition $2\epsilon_m/\omega_m = 2.6934$, $\phi = 0$, and $\omega_m = 10\Omega = (2\pi)15$MHz. (a) $\Phi^{-}(t)$. (b) $\sigma_z\Phi^{+*}(t+T/2)$. (c) $\Phi^{-*}(t+T/2)$. (d) $\Phi^{+}(t)$. (e) $\sigma_z\Phi^{-*}(t+T/2)$. (f) $\Phi^{+*}(t+T/2)$. In comparison to Fig. S1 where the parity and first particle-hole symmetries are presented, this figure presents the two discrete particle-hole symmetries under a far off-resonance condition.

Symmetry-induced transparency (siT) or coherent destruction of tunneling (CDT) are generated by destructive interference of two transition elements $V^{(n)}_{\mu,\nu} \neq 0$. In the context of light scattering, siT requires two terms in the susceptibility (Eq. S16) to cancel each other [15]:

$$V^{(-n-m)}_{\mu',\mu}V^{(m)}_{\mu,\mu'} = V^{(-n-m)}_{\mu,\mu'}V^{(m)}_{\mu',\mu}. \tag{S28}$$

In the context of coherent state evolution for our two-level system, the siT requires the amplitudes of two sidebands, at the degenerate point $\lambda^{\pm} = 0$, to destructively interfere:

$$c^{+}c^{-*}V^{(n)}_{-,+} + c^{+*}c^{-}V^{(n)}_{+,-} = 0. \tag{S29}$$

When $\Omega \ll \epsilon_m, \omega_m$, an additional particle-hole symmetry $\hat{P}_2 = \hat{P}_2^{\dagger} = I$ is introduced (as easily seen for $\Omega = 0$.) Together with the always-present particle-hole symmetry $\hat{P}_1 = \hat{P}_1^{\dagger} = \sigma_z$, we denote them as $\hat{P}_1 = \sigma_z, \hat{P}_2 = I$. Unlike $\hat{P}_1$ which maps the Floquet eigenstate to its counterpart with opposite eigenenergy, $\hat{P}_2$ maps the Floquet eigenstate to itself, with $|\Phi^{\mu}(t)\rangle = \pi^{(P_2)}_{\mu}|\Phi^{\mu*}(t+T/2)\rangle$ as shown in Fig. S8 (more detailed derivations and explanations can be found in the supplemental materials of Ref. [15]). These results can be summarized as

$$\begin{aligned}\pi^{(P_1)}_{\mu}\hat{P}_1|\Phi^{\mu*}(t+T/2)\rangle &= \left|\Phi^{\mu'}(t)\right\rangle \\ \pi^{(P_2)}_{\mu}\hat{P}_2|\Phi^{\mu*}(t+T/2)\rangle &= |\Phi^{\mu}(t)\rangle\end{aligned} \tag{S30}$$

where $\pi^{(P)}_{\mu}\pi^{(P)*}_{\mu'} = 1$, $\mu' = \mp$ for $\mu = \pm$, as derived above in Sec. III. Then the dynamical dipole matrix element is

$$\begin{aligned}V^{(n)}_{\mu,\nu} =& \frac{1}{T}\int_0^T \langle\Phi^{\mu}(t)|V|\Phi^{\nu}(t)\rangle e^{-in\omega_m t}dt = \frac{1}{T}\int_0^T \langle\Phi^{\mu*}(t+T/2)|\pi^{(P_2)*}_{\mu}\hat{P}_2^{\dagger}V\hat{P}_2\pi^{(P_2)}_{\nu}|\Phi^{\nu*}(t+T/2)\rangle e^{-in\omega_m t}dt \\ =& \alpha^{(P_2)}_V e^{i\pi n}V^{(-n)*}_{\mu,\nu} = \alpha^{(P_2)}_V e^{i\pi n}V^{(n)}_{\nu,\mu},\end{aligned} \tag{S31}$$

where $\alpha_V^{(P_2)} = 1$ since the symmetry operator is identity.

In summary, two particle-hole symmetries result in the following relations

$$V_{\mu,\nu}^{(n)} = \alpha_V^{(P_1)} e^{i\pi n} V_{\nu',\mu'}^{(n)}, \tag{S32}$$

$$V_{\mu,\nu}^{(n)} = \alpha_V^{(P_2)} e^{i\pi n} V_{\nu,\mu}^{(n)} = e^{i\pi n} V_{\nu,\mu}^{(n)}. \tag{S33}$$

As discussed in Sec. III, the selection rules for the sidebands induced by the first particle-hole symmetry $\hat{P}_1 = \sigma_z$ are already included in the parity symmetry prediction, and destructive (or constructive) interference happens for the centerbands when the initial state is an equal superposition of Floquet eigenstates. Considering the second particle-hole symmetry $\hat{P}_2 = I$, destructive (or constructive) interference happens in the sidebands when they have the same frequency (degenerate condition $\lambda^{\pm} = 0$).

1. When $c^+ c^{-*} = c^{+*} c^-$ (e.g., initial state $|0\rangle$, modulation phase $\phi = 0$ or $\phi = \pi/2$), destructive interference happens for the odd bands with $e^{i\pi n} = -1$, which is observed in simulation shown in Figs. S9(b,f) where a clear siT happens at $2\epsilon_m/\omega_m = 2.4048$.

2. When $c^+ c^{-*} = -c^{+*} c^-$ (e.g., initial state $|+i\rangle$, modulation phase $\phi = \pi/2$), constructive interference happens for the odd bands with $e^{i\pi n} = -1$, which is observed in simulation shown in Figs. S10(b,f).

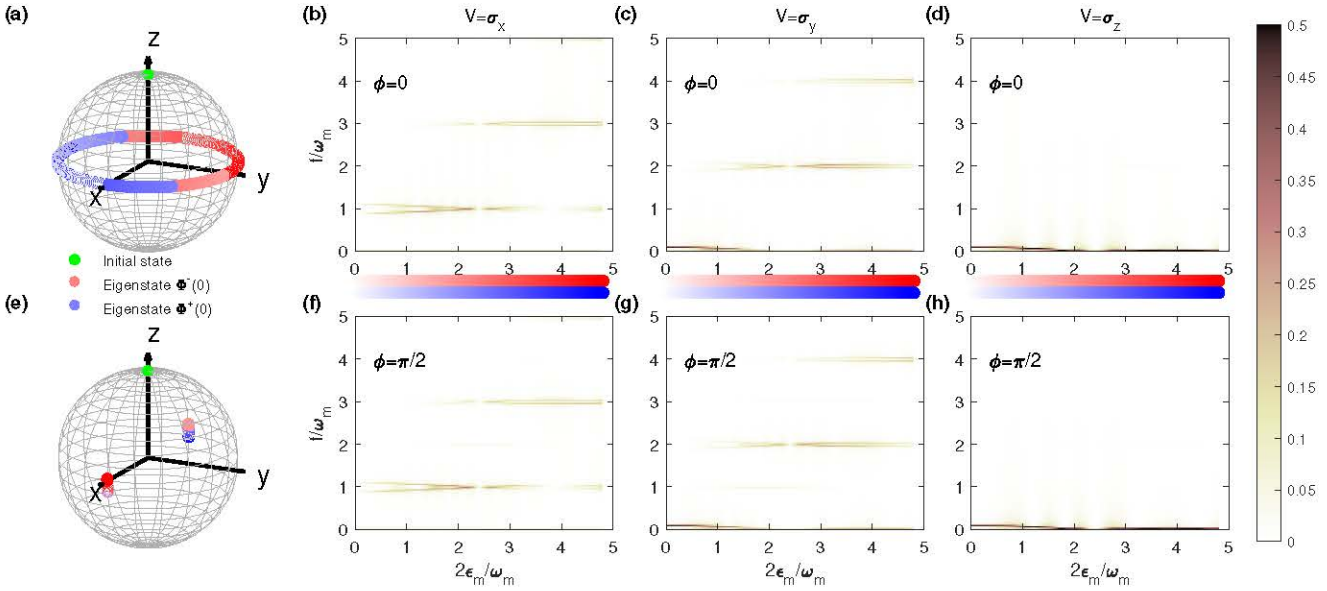

FIG. S9. Simulation of siT, aDS and spDS under a strong coupling regime. Qubit initial state is prepared to $|0\rangle$ and the Rabi oscillations are simulated from $t = 0$ to $t = 2\mu$s. Parameters are $\Omega = (2\pi)1.5$MHz, $\omega_m = (2\pi)15$MHz, $\phi = 0, \pi/2$. (a,e) Visualization of Floquet eigenstates $|\Phi^{\pm}(0)\rangle$ on the Bloch sphere. The color change from white to red or blue as the increase of $2\epsilon_m/\omega_m$ from 0 to 4.8096. (b,f) Fourier spectrum of Rabi measurement on $|+\rangle$ ($V = \sigma_x$) under different modulation strength $2\epsilon_m/\omega_m$. (c,g) Fourier spectrum of Rabi measurement on $|+i\rangle$ ($V = \sigma_y$) under different modulation strength $2\epsilon_m/\omega_m$. (d,h) Fourier spectrum of Rabi measurement on $|0\rangle$ ($V = \sigma_z$) under different modulation strength $2\epsilon_m/\omega_m$.

We also perform experiments to observe both the destructive and constructive interferences with different qubit initial states (Fig. S11.) When the qubit initial state is $|0\rangle$, such that $c^+ c^{-*} = c^{+*} c^-$, and $V_{+,-}^{(n)} = -V_{+,-}^{(n)}$ at $2\epsilon_m/\omega_m = 2.4048$, a destructive interference between two sidebands happens and siT or CDT are observed in Fig. S11(a). However, when the qubit initial state is prepared to $|+i\rangle$ such that $c^+ c^{-*} = -c^{+*} c^-$, a constructive interference happens at the degeneracy point as observed in Fig. S11(b).

In both derivations of Eq. (S27) and Eq. (S31), the observation operator needs to satisfy $\hat{P}^\dagger V \hat{P} = \alpha_V^{(P)} V^*$. Thus, the previous derivations do not predict the situation of $V = \sigma_y$. However, siT is also observed for $V = \sigma_y$ as shown in simulation in Figs. S9(c,g). We show in the following that siT can be also observed when the probe operator is σ_y, thanks to particle-hole symmetry.

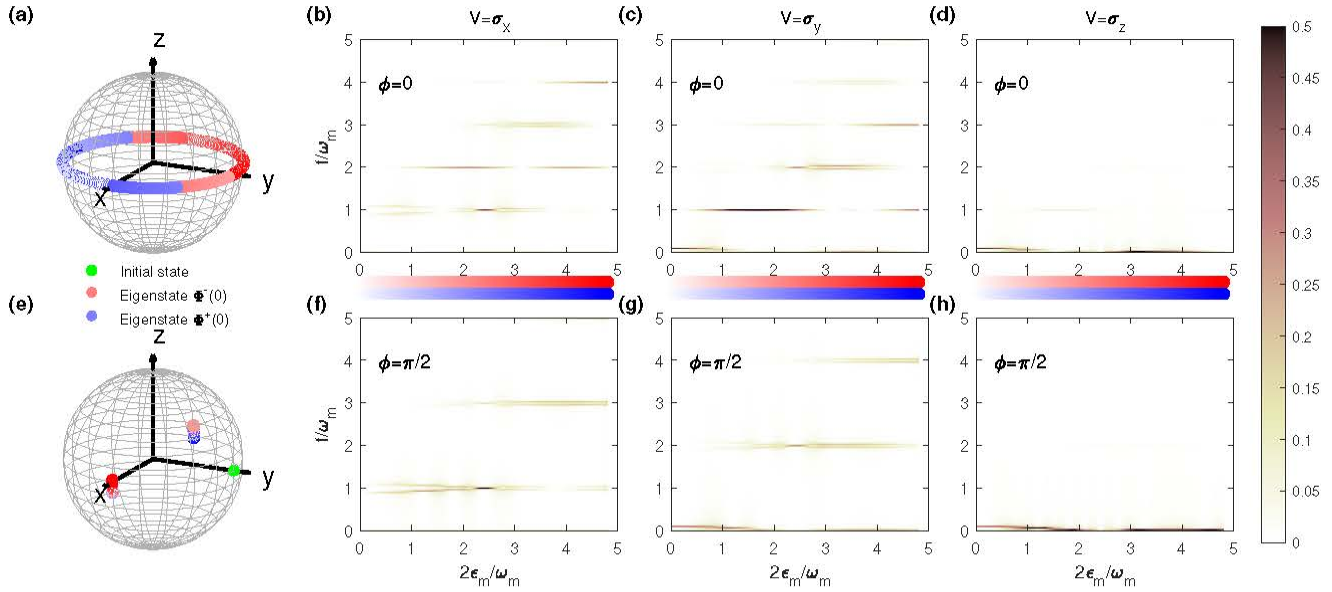

FIG. S10. Simulation of siT, aDS, spDS and spDB under a strong coupling regime. Qubit initial state is prepared to $|+i\rangle$ (the eigenstate of σ_y) and the Rabi oscillations are simulated from $t = 0$ to $t = 2\mu$s. Parameters are $\Omega = (2\pi)1.5$MHz, $\omega_m = (2\pi)15$MHz, $\phi = 0, \pi/2$. (a,e) Visualization of Floquet eigenstates $|\Phi^{\pm}(0)\rangle$ on the Bloch sphere. The color change from white to red or blue as the increase of $2\epsilon_m/\omega_m$ from 0 to 4.8096. (b,f) Fourier spectrum of Rabi measurement on $|+\rangle$ ($V = \sigma_x$) under different modulation strength $2\epsilon_m/\omega_m$. (c,g) Fourier spectrum of Rabi measurement on $|+i\rangle$ ($V = \sigma_y$) under different modulation strength $2\epsilon_m/\omega_m$. (d,h) Fourier spectrum of Rabi measurement on $|0\rangle$ ($V = \sigma_z$) under different modulation strength $2\epsilon_m/\omega_m$.

Here we combine both particle-hole symmetries in the derivation and calculate the dynamical dipole matrix element:

$$\begin{aligned} V^{(n)}_{\mu,\nu} =& \frac{1}{T}\int_0^T \langle \Phi^{\mu}(t)|V|\Phi^{\nu}(t)\rangle e^{-in\omega_m t}dt = \frac{1}{T}\int_0^T \langle \Phi^{\mu *}(t+T/2)|\pi^{(P_2)*}_{\mu}\hat{P}_2^{\dagger}V\hat{P}_2\pi^{(P_2)}_{\nu}|\Phi^{\nu *}(t+T/2)\rangle e^{-in\omega_m t}dt \\ =& \frac{1}{T}\int_0^T \langle \Phi^{\mu'}(t+T)|\hat{P}_1^{\dagger *}\pi^{(P_1)}_{\nu'}\pi^{(P_2)*}_{\mu}\hat{P}_2^{\dagger}V\hat{P}_2\pi^{(P_2)}_{\nu}\pi^{(P_1)*}_{\mu'}\hat{P}_1^{*}|\Phi^{\nu'}(t+T)\rangle e^{-in\omega_m t}dt \\ =& \alpha_V^{(P_1^*)}V^{(n)}_{\mu',\nu'}, \end{aligned} \tag{S34}$$

where $\pi^{(P)}_{\mu}\pi^{(P)*}_{\nu} = 1, \hat{P}_2 = I$ are used and $\alpha_V^{(P_1^*)}$ is given by $\alpha_V V = \hat{P}_1^{\dagger *}V\hat{P}_1^{*}$. Since $\hat{P}_1 = \hat{P}_1^{*} = \sigma_z$, then $\alpha_V^{(P_1^*)} = -1$ and $V^{(n)}_{+,-} = -V^{(n)}_{-,+}$ for both $V = \sigma_x, \sigma_y$ and destructive interference happens for both situations. Note that here we do not require $V = V^*$.

Under the siT condition, the transition between $|0\rangle$ and $|1\rangle$ is suppressed, a phenomenon which is also called *coherent destruction of tunneling* (CDT). To further visualize this exotic phenomenon, we plot the state evolution on the Bloch sphere under four different conditions $\omega_m = 2\Omega, 6\Omega, 10\Omega, 20\Omega$ in Figs. S12(a,b,c,d) with their corresponding Rabi oscillations in Figs. S12(e,f,g,h). From the comparison, we can see that as Ω/ω_m decreases, the second particle-hole symmetry becomes progressively prominent, and the transition between $|0\rangle$ and $|1\rangle$ is more suppressed, as predicted by the symmetry analysis.

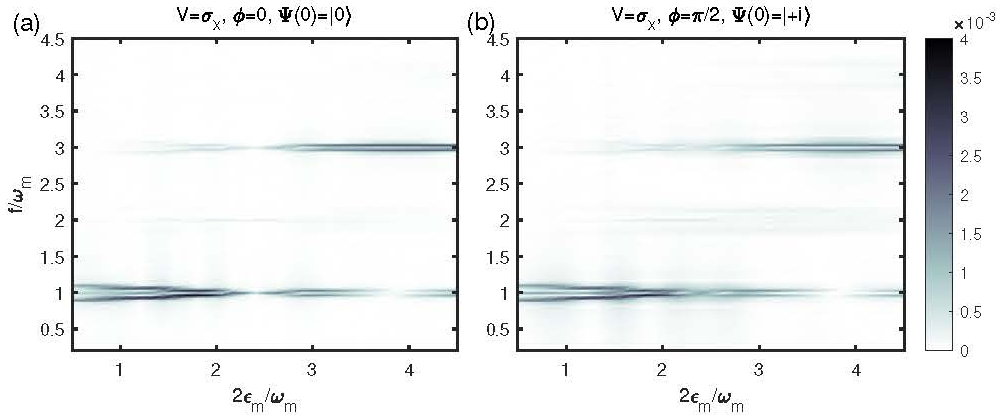

FIG. S11. Experimental observation of siT, aDS, spDS, and spDB under a strong coupling regime. (a) Qubit initial state is prepared to $|0\rangle$ and the time-dependent population on $|+\rangle$ is readout ($V = \sigma_x$) from $t = 0$ to $t = 2\mu$s. Driving parameters are $\Omega = (2\pi)1.5$MHz, $\omega_m = (2\pi)15$MHz, $\phi = 0$. The intensity plot is the Fourier spectrum of measured Rabi oscillations under different ϵ_m. (b) Same experiment as (a) except for the initial state $|+i\rangle$ (eigenstate of σ_y) and the modulation phase $\phi = \pi/2$.

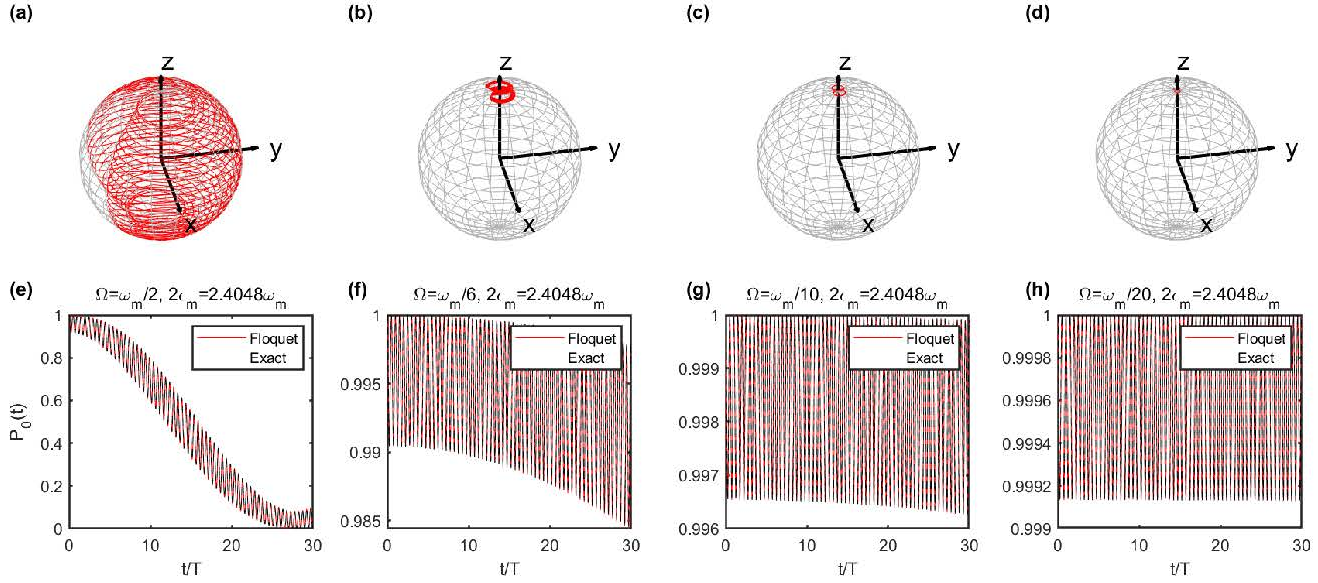

FIG. S12. Simulation of siT (CDT) under different Ω. Parameters are $\omega_m = (2\pi)15$MHz, $\phi = 0, 2\epsilon_m/\omega_m = 2.4048$ and the qubit evolutions of an initial state $|0\rangle$ are plotted on Bloch sphere in (a-d) and population on $|0\rangle$ is plotted in (e-h) (a,e) $\Omega = \omega_m/2$. (b,f) $\Omega = \omega_m/6$. (c,g) $\Omega = \omega_m/10$. (d,h) $\Omega = \omega_m/20$.

V. ROTATION SYMMETRY IN A 3-LEVEL SYSTEM

A. Hamiltonian engineering by amplitude or phase modulation

In this section we introduce a novel method that exploits simultaneous modulated driving of various transitions as a playground to study rotation symmetry. In particular, focusing on the NV center in diamond, here we show that even with just two modulated microwave drivings, all three energy levels can be directly coupled in the rotating frame.

Amplitude modulation - The NV center ground state Hamiltonian in the lab frame under simultaneous driving of the transitions between $|m_s=0\rangle$ and $|m_s=\pm1\rangle$ is

$$H=\gamma BS_z+DS_z^2+\sqrt{2}\left[\Omega_1\cos(\omega_1 t)-2\epsilon_{m1}(t)\sin(\omega_1 t)+\Omega_2\cos(\omega_2 t)+2\epsilon_{m2}(t)\sin(\omega_2 t)\right]S_x \tag{S35}$$

We consider identical detuning for both transitions $\Delta=\omega_{1(2)}-(D\pm\gamma B)$ (here D is the NV zero-field splitting, B the magnetic field and γ the gyromagnetic ratio). In the rotating frame defined by $U_1=\mathrm{diag}(e^{-i\omega_1 t},0,e^{-i\omega_2 t})$, under the rotating wave approximation we obtain

$$\tilde{H}=\begin{pmatrix}0 & \frac{\Omega_1}{2}-i\epsilon_{m1}(t) & 0\\ \frac{\Omega_1}{2}+i\epsilon_{m1}(t) & \Delta & \frac{\Omega_2}{2}-i\epsilon_{m2}(t)\\ 0 & \frac{\Omega_2}{2}-i\epsilon_{m2}(t) & 0\end{pmatrix}, \tag{S36}$$

where a constant term (energy shift) $\mathrm{diag}(-\Delta,-\Delta,-\Delta)$ is neglected. While the relation between the detuning Δ and the driving strength $\Omega_{1(2)}$ can be tuned over a broad range, here we set $\Omega_1=\Omega_2=2\Delta$. We then diagonalize the static part of Eq. S36:

$$\tilde{H}_T=\begin{pmatrix}2\Delta & -i\frac{\epsilon_{m1}(t)+\epsilon_{m2}(t)}{\sqrt{3}} & i\frac{\epsilon_{m1}(t)-\epsilon_{m2}(t)}{\sqrt{2}}\\ i\frac{\epsilon_{m1}(t)+\epsilon_{m2}(t)}{\sqrt{3}} & 0 & -i\frac{\epsilon_{m1}(t)+\epsilon_{m2}(t)}{\sqrt{6}}\\ -i\frac{\epsilon_{m1}(t)-\epsilon_{m2}(t)}{\sqrt{2}} & i\frac{\epsilon_{m1}(t)+\epsilon_{m2}(t)}{\sqrt{3}} & -\Delta\end{pmatrix}. \tag{S37}$$

To reach the target Hamiltonian which has the same driving strengths but different phases between all the three energy levels, we set the modulations to be

$$\epsilon_{m1}(t)=2\sqrt{3}J\sin(2\Delta t)\cos\left(\omega_m t+\frac{2\pi}{3}\right)-2\sqrt{2}J\sin(3\Delta t)\cos(\omega_m t),\quad \epsilon_{m2}(t)=2\sqrt{6}J\sin(\Delta t)\cos\left(\omega_m t+\frac{4\pi}{3}\right). \tag{S38}$$

Under the rotating frame defined by $U_2=\mathrm{diag}(e^{-i2\Delta t},0,e^{i\Delta t})$, we finally obtain

$$\mathcal{H}_I=\begin{pmatrix}0 & J\cos\left(\omega_m t+\frac{2\pi}{3}\right) & J\cos(\omega_m t)\\ J\cos\left(\omega_m t+\frac{2\pi}{3}\right) & 0 & J\cos\left(\omega_m t+\frac{4\pi}{3}\right)\\ J\cos(\omega_m t) & J\cos\left(\omega_m t+\frac{4\pi}{3}\right) & 0\end{pmatrix}. \tag{S39}$$

Note that here we use the rotating wave approximation which holds when $\Delta\gg\omega_m, J$ (see Fig. S14(c) for a symmetry breakdown caused by the neglected fast oscillating terms in this approximation). The period of this Hamiltonian is $T=2\pi/\omega_m$.

Phase modulation - An alternative way to engineer a similar Hamiltonian is by phase modulation, where two phase modulated microwaves are applied to the transition between $|m_s=0\rangle$ and $|m_s=\pm1\rangle$. Again we start from the Hamiltonian in the lab frame

$$H=\gamma BS_z+DS_z^2+\sqrt{2}\left[\Omega_1\cos(\omega_1 t+f_1(t))+\Omega_2\cos(\omega_2 t+f_2(t))\right]S_x, \tag{S40}$$

with identical detuning for both transitions $\Delta=\omega_{1(2)}-(D\pm\gamma B)$. In the rotating frame defined by $U_1=\mathrm{diag}(e^{-i(\omega_1 t+f_1(t))},0,e^{-i(\omega_2 t+f_2(t))})$, under the rotating wave approximation we reach

$$\tilde{H}=\begin{pmatrix}\epsilon_{m1}(t) & \frac{\Omega_1}{2} & 0\\ \frac{\Omega_1}{2} & \Delta & \frac{\Omega_2}{2}\\ 0 & \frac{\Omega_2}{2} & \epsilon_{m2}(t)\end{pmatrix}, \tag{S41}$$

where a constant term diag$(-\Delta,-\Delta,-\Delta)$ is neglected, and $\epsilon_{m1(2)} = -\frac{d}{dt}f_{1(2)}(t)$. Setting again $\Omega_1/2 = \Omega_2/2 = \Delta$ and diagonalizing the static part of Eq. (S41), we obtain

$$\tilde{H}_T = \begin{pmatrix} 2\Delta + \frac{\epsilon_{m1}(t)+\epsilon_{m2}(t)}{6} & \frac{-\epsilon_{m1}(t)+\epsilon_{m2}(t)}{2\sqrt{3}} & \frac{\epsilon_{m1}(t)+\epsilon_{m2}(t)}{3\sqrt{2}} \\ \frac{-\epsilon_{m1}(t)+\epsilon_{m2}(t)}{2\sqrt{3}} & \frac{\epsilon_{m1}(t)+\epsilon_{m2}(t)}{2} & \frac{-\epsilon_{m1}(t)+\epsilon_{m2}(t)}{\sqrt{6}} \\ \frac{\epsilon_{m1}(t)+\epsilon_{m2}(t)}{3\sqrt{2}} & \frac{-\epsilon_{m1}(t)+\epsilon_{m2}(t)}{\sqrt{6}} & -\Delta + \frac{\epsilon_{m1}(t)+\epsilon_{m2}(t)}{3} \end{pmatrix}. \tag{S42}$$

To reach the target Hamiltonian, Eq. (S39), we set the modulation to be

$$\epsilon_{m1}(t) = -4\sqrt{3}J\sin(2\Delta t)\cos\left(\omega_m t + \frac{2\pi}{3}\right) + 6\sqrt{2}J\sin(3\Delta t)\cos(\omega_m t), \quad \epsilon_{m2}(t) = 2\sqrt{6}J\sin(\Delta t)\cos\left(\omega_m t + \frac{4\pi}{3}\right). \tag{S43}$$

Under the rotating frame defined by $U_2 = diag(e^{-i2\Delta t}, 0, e^{i\Delta t})$, we finally get the same Hamiltonian as in Eq. (S39). Note that here we also use the similar rotating wave approximation.

B. Symmetry protected selection rules

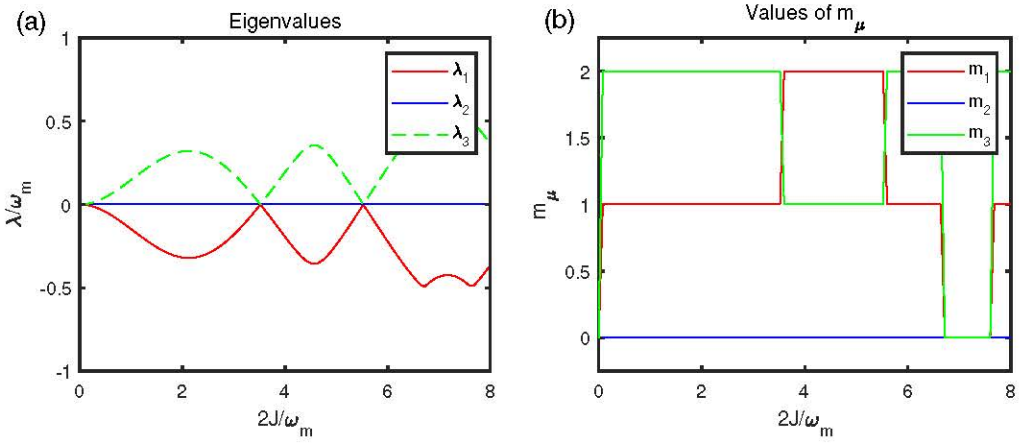

FIG. S13. Floquet eigenenergies and π_μ. (a) Floquet eigenenergies $\lambda^{1,2,3}$. Note that λ is defined in the range $(-\omega_m/2, \omega_m/2]$ and $\lambda^1 \leq \lambda^2 \leq \lambda^3$. (b) The values of $m_{1,2,3}$ corresponding to the rotation symmetry. Floquet simulations in this figure are implemented under the condition $\omega_m = (2\pi)0.3$MHz.

The symmetry associated with the Hamiltonian $\mathcal{H}_I$ in Eq. (S39) is a 3-fold rotation symmetry

$$\hat{R} = \begin{pmatrix} 0 & 0 & 1 \\ 1 & 0 & 0 \\ 0 & 1 & 0 \end{pmatrix}, \tag{S44}$$

which simply gives $\hat{R}\mathcal{H}_I(t+T/3)\hat{R}^\dagger = \mathcal{H}_I(t)$. Such a symmetry gives rise to a relation among eigenstates, $|\Phi^\mu(t)\rangle = \pi_\mu^{(R)}\hat{R}\,|\Phi^\mu(t+T/3)\rangle = e^{i2\pi m_\mu/3}\hat{R}\,|\Phi^\mu(t+T/3)\rangle$ with $\mu \in \{1,2,3\}$ and $m_\mu \in \{0,1,2\}$ [15]. The values of $\pi_\mu^{(R)} = e^{i2\pi m_\mu/3}$ depend on the driving parameter J (also on how we define the bands). In Figs. S13(b), we simulate and plot the three values of $m_{1,2,3}$ as a function of $2J/\omega_m$ where $m_{1,3}$ switch with each other when their eigenvalues cross the degeneracy point.

Now we derive the selection rules by evaluating the value of the dynamical dipole matrix element,

$$\begin{aligned} V_{\mu,\nu}^{(n)} &= \frac{1}{T}\int_0^T \langle\Phi^\mu(t)|V|\Phi^\nu(t)\rangle e^{-in\omega_m t}dt \\ &= \frac{1}{T}\int_0^{T/3} \langle\Phi^\mu(t)|V|\Phi^\nu(t)\rangle e^{-in\omega_m t}dt \times \left[1 + \pi_\mu^{(R)}\pi_\nu^{(R)*}e^{-i\frac{2\pi}{3}n}\alpha_V + \left(\pi_\mu^{(R)}\pi_\nu^{(R)*}e^{-i\frac{2\pi}{3}n}\alpha_V\right)^2\right], \end{aligned} \tag{S45}$$

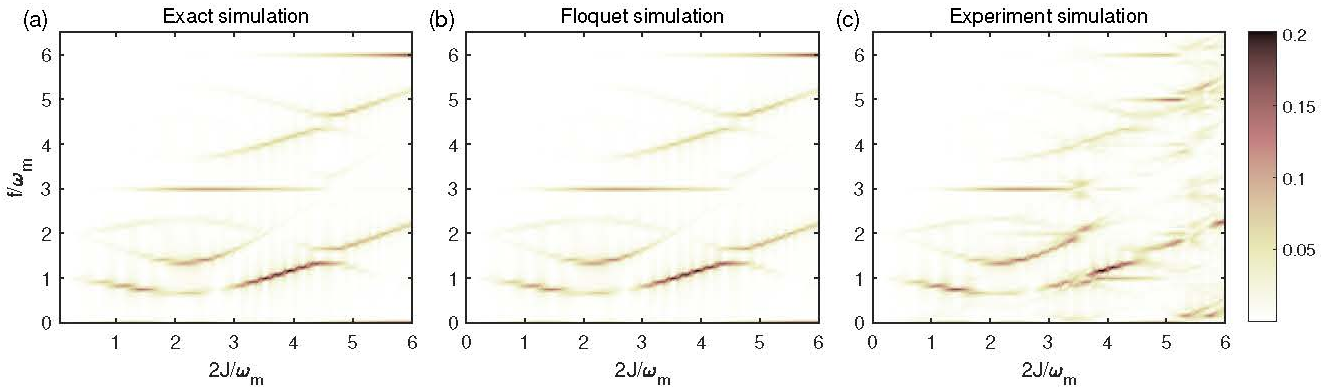

FIG. S14. Simulation of spDSs and spDBs in a 3-level system. The initial state is prepared to $(1/\sqrt{3})(|e_1\rangle + |e_2\rangle + |e_3\rangle)$ where $|e_1\rangle = (1/\sqrt{3})[1,1,1]^T$, $|e_2\rangle = (1/\sqrt{6})[-2,1,1]^T$, $|e_3\rangle = (1/\sqrt{2})[0,1,-1]^T$ are three eigenstates of V, such that evolution mode involves all bands. Driving parameters $\omega_m = (2\pi)0.3$MHz, and $2J/\omega_m$ is swept from 0 to 6. The intensity plot is the Fourier spectrum of simulated Rabi oscillations under different $2J/\omega_m$. (a) Exact simulation. The time-dependent weighted Rabi population $P(t)$ is simulated from $t = 0$ to $t = 40\mu$s with 5001 sampling points. Hamiltonian in Eq. (S39) is used to calculate the exact evolution. (b) Floquet simulation. The Floquet matrix is truncated to a 300 blocks by 300 blocks, the evolution time is swept from $t = 0$ to $t = 40\mu$s with 5001 sampling points. (c) Experiment simulation. Hamiltonian in the first rotating frame in Eq. (S36) is used where $\Omega_1 = \Omega_2 = 2\Delta = (2\pi)30$ MHz is used. The time-dependent weighted Rabi population $P(t)$ is simulated from $t = 0$ to $t = 40\mu$s with 160001 sampling points to achieve high precision.

where the value of α_V is given by the relation $\hat{R}V\hat{R}^\dagger = \alpha_V V$. Since α_V, $\pi_\mu^{(R)}$ and $\pi_\nu^{(R)}$ can only take values from $\{e^{i\frac{2\pi}{3}}, e^{i\frac{4\pi}{3}}, 1\}$ due to their 3-fold rotational symmetry, the band vanishing condition is that $e^{i\frac{2\pi}{3}(m_\mu - m_\nu - n)}\alpha_V \neq 1$, which is validated in the simulation shown in the main text as well as in supplementary Fig. S14.

In this work, we evaluate the observation operator

$$V = \begin{pmatrix} 0 & 1 & 1 \\ 1 & 0 & 1 \\ 1 & 1 & 0 \end{pmatrix}, \tag{S46}$$

which gives $\alpha_V = 1$. This observation operator can be rewritten in its eigen-basis as $V = 2|e_1\rangle\langle e_1| - |e_2\rangle\langle e_2| - |e_3\rangle\langle e_3|$ where $|e_1\rangle = (1/\sqrt{3})[1,1,1]^T$, $|e_2\rangle = (1/\sqrt{6})[-2,1,1]^T$, $|e_3\rangle = (1/\sqrt{2})[0,1,-1]^T$. Thus, the weighted Rabi signal is defined as $P(t) = (1/4)\left[2P_{|e_1\rangle}(t) - P_{|e_2\rangle}(t) - P_{|e_3\rangle}(t)\right]$. The Fourier spectrum of this signal presenting the spDSs and spDBs is shown in both the main text and in Fig. S14.

We notice that due to the relation $\lambda_3 = -\lambda_1$ as shown in Fig. S13(a), the sideband degenerate conditions $\omega_{3,2}^{(n)} = \omega_{2,1}^{(n)}$ and $\omega_{2,3}^{(n)} = \omega_{1,2}^{(n)}$ are always satisfied. Due to the equality $\pi_2^{(R)}\pi_3^{(R)*} = \pi_1^{(R)}\pi_2^{(R)*}$ as validated in Fig. S13(b), the selection rules for spDSs are the same for degenerate bands. In the main text plot, we only label each band with one frequency to avoid confusion. We note that the interference of these degenerate bands cannot be clearly observed under the initial state we choose in the simulation, $|\Psi(0)\rangle = (|e_1\rangle + |e_2\rangle + |e_3\rangle)/\sqrt{3}$, due to $|c^{2*}c^3| \neq |c^{1*}c^2|$.

To further mimic a practical experiment, we perform the exact simulation in the first rotating frame [Eq. (S36)], where fast oscillating terms at harmonics of frequency Δ are not neglected as in Eq. (S39). We take the parameters $\omega_m = (2\pi)0.3$ MHz, $\Delta = \Omega_1/2 = \Omega_2/2 = (2\pi)15$ MHz, and show the result in Fig. S14(c). In comparison to both exact and Floquet simulations in Figs. S14(a,b), some protected spDSs or spDBs start to appear at larger J when the rotating wave approximation starts to break down.

VI. EXPERIMENTAL IMPERFECTIONS

In the comparison between the experimental data in Fig. S3 and exact simulations in Fig. S4, we find that some unexpected centerbands are observed experimentally, which are forbidden by the selection rules. Since we are using a qubit ensemble with 10^{10} qubits being addressed simultaneously, the dominant noise comes from field inhomogeneities as discussed in detail in Ref. [14]. One possible reason for these unexpected bands is that the inhomogeneities introduce a detuning term $(\delta/2)\sigma_z$ in the Hamiltonian $\mathcal{H}_I$, which breaks both parity and particle-hole symmetries. In Fig. S15, we simulate this effect assuming a normal distribution of the detuning term $\delta \sim \mathcal{N}(0, (2\pi)0.15\text{MHz})$, and the simulation shows the appearance of the unexpected centerbands and also sidebands. Since the centerband is highly robust against experimental noise and other imperfections as studied in Ref. [14], the unexpected centerbands are more prominent than the sidebands.

A second experimental imperfection arises from the coupling to the ^{14}N nuclear spin ($m_I = 0, \pm 1$) with hyperfine coupling constant $A = (2\pi)2.16\text{MHz}$. Under the experimental conditions, where the magnetic field is 239G, only $\sim 70\%$ of the NV spin is polarized in the hyperfine level $m_I = +1$ (which is the state we assume in this work), and there are still 30% NV spins with detunings $A = (2\pi)2.16\text{MHz}$, $2A = (2\pi)4.32\text{MHz}$. These static detunings break the same dynamical symmetries and could also induce the unexpected bands.

A third experimental imperfection is due to the nonlinearity of the microwave amplifier. In the supplemental materials of Ref. [1], we characterize the nonlinearity of the microwave amplifier in the same experimental setup and show that such nonlinearity may induce higher harmonics which affect the engineered Hamiltonian.

A fourth experimental imperfection arises from the fact that the microwave field also has a longitudinal component which gives rise to an additional σ_z term in the lab frame Hamiltonian which breaks the aforementioned symmetries.

Finally, the Hamiltonian $\mathcal{H}_I$ was derived under the rotating wave approximation. For strong driving, counter-rotating terms may also induce symmetry breaking, as validated by the comparison in Fig. S14, where the simulation performed using the Hamiltonian in the first rotating frame in Fig. S14(c) causes symmetry breaking, while the simulation with the Hamiltonian in the second rotating frame (where the RWA has been applied) in Fig. S14(a) and (b) does not show any symmetry breaking.

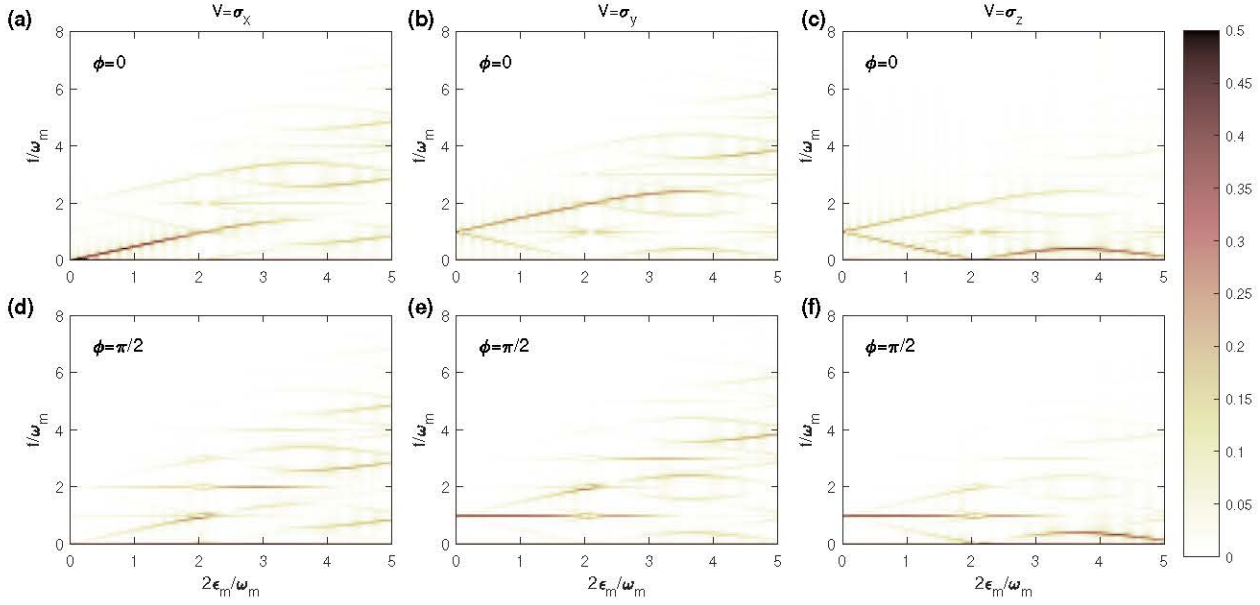

FIG. S15. Simulation of symmetry breaking due to inhomogeneities. Parameters are the same as in Fig. S4 except for assuming a Normal distribution of the detuning $\delta \sim \mathcal{N}(0, \sigma = (2\pi)0.15\text{MHz})$ in Hamiltonian $\mathcal{H}_I = (\delta/2)\sigma_z + (\Omega/2)\sigma_x + \epsilon_m \sin(\omega_m t + \phi)\sigma_z$. To simplify the simulation, we sample 51 points from $\delta = -2\sigma$ to $\delta = 2\sigma$ and calculate their average Rabi signals.

Even if these experimental imperfections might be obfuscating the results, there are several strategies to separate their effects from the physics of interest.

1. As done in our experiments, one can exploit the modulated driving technique to engineer any desired symmetry breaking Hamiltonian. Then, by comparing the band amplitudes with and without symmetry breaking, one can deduce the bands that are protected by the symmetries. This strategy can be further used to study different types of symmetry breakings, e.g., the inhomogeneities-induce symmetry breaking by adding a static σ_z term,

the symmetry breaking induced by electronics imperfections such as power saturation through higher harmonic driving terms. Since different symmetry breakings might induce different features in the Rabi spectra, they can also be utilized to characterize the imperfections of any quantum devices, especially in combination with simulation.

2. The modulated driving technique can be implemented by many different schemes that display different imperfections. For example, amplitude modulation suffers more from power saturation due to large amplitude variation, while the phase modulation is more affected by phase noise due to limited time resolution of arbitrary waveform generators. Finally, one could add another input source to apply the σ_z driving in the lab frame without any need for modulation, which potentially has better performance than modulation methods. By comparing results using different techniques one can extract the interesting physics from effects due to imperfection and further pinpoint the best method for a given experimental condition.

VII. EXPERIMENTAL SETUP

In Fig. S16, we show a simplified schematic of our experimental setup. An IQ mixer mixes a low frequency signal ($\sim$ 100 MHz) generated by an arbitrary waveform generator (AWG) with a high frequency signal ($\sim$ 2.1 GHz) generated by a signal generator, to apply the quantum control. The phase-modulated CCD is implemented through MATLAB coding of the AWG. The mixed microwave signal is further delivered to the diamond through a loop structure on a PCB board. The fluorescence signal is collected by three photodiodes, which connect to a data acquisition card. The laser path is controlled by an acousto-optic modulator (AOM). A pulse blaster (PulseBlasterESR-PRO 500) is used to apply synchronized gates to electronics and optics. We apply an external magnetic field 239 G to the sample. The field strength is chosen as a compromise between achieving efficient polarization of the nitrogen nuclear spin and reducing field inhomogeneities on the spin ensemble.

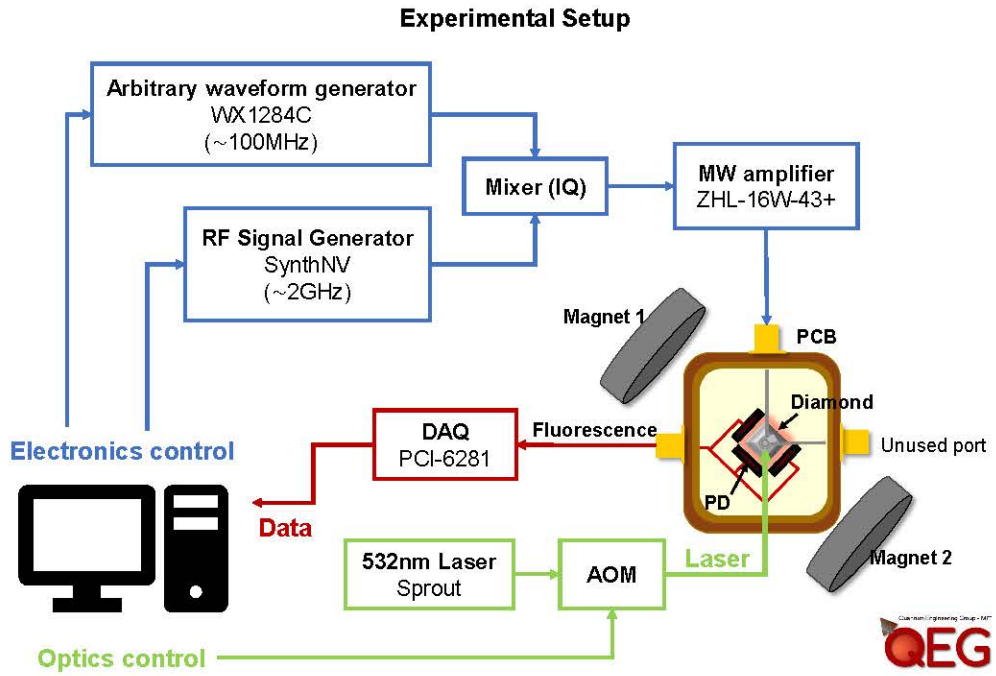

FIG. S16. Simplified schematic of the experimental setup.

[1] G. Wang, Y.-X. Liu, and P. Cappellaro, Phys. Rev. A **103**, 022415 (2021).
[2] M. Leskes, P. Madhu, and S. Vega, Prog Nucl Mag Res Sp **57**, 345 (2010).

[3] J.-M. Cai, B. Naydenov, R. Pfeiffer, L. P. McGuinness, K. D. Jahnke, F. Jelezko, M. B. Plenio, and A. Retzker, New J. Phys. **14**, 113023 (2012).
[4] N. Khaneja, A. Dubey, and H. S. Atreya, J. Mag. Res. **265**, 117 (2016).
[5] A. Saiko, R. Fedaruk, and S. Markevich, J. Mag. Res. **290**, 60 (2018).
[6] I. Cohen, N. Aharon, and A. Retzker, Fortschr. Phys. **65**, 1600071 (2017).
[7] D. Farfurnik, N. Aharon, I. Cohen, Y. Hovav, A. Retzker, and N. Bar-Gill, Phys. Rev. A **96**, 013850 (2017).
[8] S. Rohr, E. Dupont-Ferrier, B. Pigeau, P. Verlot, V. Jacques, and O. Arcizet, Phys. Rev. Lett. **112**, 010502 (2014).
[9] K. J. Layton, B. Tahayori, I. M. Mareels, P. M. Farrell, and L. A. Johnston, J. Mag. Res. **242**, 136 (2014).
[10] A. P. Saiko, R. Fedaruk, and S. A. Markevich, J. Mag. Res. **259**, 47 (2015).
[11] J. Teissier, A. Barfuss, and P. Maletinsky, J. Opt. **19**, 044003 (2017).
[12] S. Bertaina, H. Vezin, H. De Raedt, and I. Chiorescu, Sci. Rep. **10**, 21643 (2020).
[13] Q.-Y. Cao, P.-C. Yang, M.-S. Gong, M. Yu, A. Retzker, M. Plenio, C. Müller, N. Tomek, B. Naydenov, L. McGuinness, F. Jelezko, and J.-M. Cai, Phys. Rev. Appl. **13**, 024021 (2020).
[14] G. Wang, Y.-X. Liu, and P. Cappellaro, New J. Phys. **22**, 123045 (2020).
[15] G. Engelhardt and J. Cao, Phys. Rev. Lett. **126**, 090601 (2021).